AD-A182 776 SYNTHETIC APERTURE RADAR OCEANOGRAPHIC INVESTIGATIONS (U) ENVIRONMENTAL RESEARCH INST OF MICHIGAN ANN ARBOR RADAR SCIENCE LAB D R LYZENGA ET AL 01 MAR 87 1/1

UNCLASSIFIED ERIM-155900-62-T N00014-81-C-0692 F/G 17/9 NL

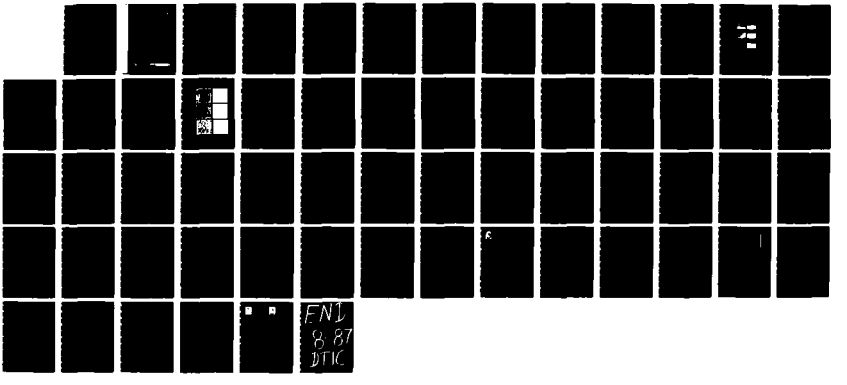

END
8 87
DTIC

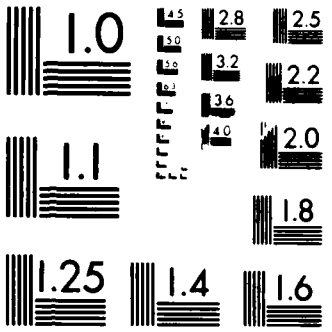

(12)

155900-62-T

Technical Report

SYNTHETIC APERTURE RADAR OCEANOGRAPHIC INVESTIGATIONS

D.R. LYZENGA
R.A. SHUCHMAN
Radar Science Laboratory
Advanced Concept Division

FEBRUARY 1987

NASA Headquarters
600 Independence Avenue
Washington, D.C. 20546
Contract No. N00014-81-C-0692
Technical Monitor: James Richman

ERIM P.O. Box 8618 Ann Arbor, MI 48107-8618

Unclassified
SECURITY CLASSIFICATION OF THIS PAGE

REPORT DOCUMENTATION PAGE

1a. REPORT SECURITY CLASSIFICATION Unclassified	1b. RESTRICTIVE MARKINGS None
2a. SECURITY CLASSIFICATION AUTHORITY	3. DISTRIBUTION/AVAILABILITY OF REPORT Unlimited
2b. DECLASSIFICATION/DOWNGRADING SCHEDULE	
4. PERFORMING ORGANIZATION REPORT NUMBERS(S) 155900-62-T	5. MONITORING ORGANIZATION REPORT NUMBER(S) UPN 161-85-10-04 (1873-OP-326)
6a. NAME OF PERFORMING ORGANIZATION Environmental Research Institute of Michigan 6b. OFFICE SYMBOL *(if applicable)*	7a. NAME OF MONITORING ORGANIZATION Technical Monitor: James Richman
6c. ADDRESS (City, State, and ZIP Code) P.O. Box 8618 Ann Arbor, MI 48107	7b. ADDRESS (City, State, and ZIP Code)
8a. NAME OF FUNDING /SPONSORING ORGANIZATION NASA Headquarters 8b. OFFICE SYMBOL *(if applicable)*	9. PROCUREMENT INSTRUMENT IDENTIFICATION NUMBER N00014-81-C-0692
8c. ADDRESS (City, State, and ZIP Code) 600 Independence Avenue Washington, DC 20546	10. SOURCE OF FUNDING NUMBERS PROGRAM ELEMENT NO. / PROJECT NO. / TASK NO. / WORK UNIT ACCESSION NO.

11. TITLE (Include Security Classification)
Synthetic Aperture Radar Oceanographic Investigations

12. PERSONAL AUTHOR(S)
David R. Lyzenga, Robert A. Shuchman

13a. TYPE OF REPORT	13b. TIME COVERED	14. DATE OF REPORT (Year, Month, Day)	15. PAGE COUNT
Technical	FROM 8/85 TO 2/87	1 March 1987	ii +

16. SUPPLEMENTARY NOTATION

17. COSATI CODES			18. SUBJECT TERMS *(Continue on reverse if necessary and identify by block number)*
FIELD	GROUP	SUB-GROUP	

19. ABSTRACT *(Continue on reverse if necessary and identify by block number)*

ABSTRACT

This report summarizes recent progress in the application of synthetic aperture radar (SAR) to several oceanographic measurement problems. Limitations of conventional (i.e., strip-map) SAR systems are analyzed and the possible advantages of several non-conventional or advanced SAR configurations are discussed. These non-conventional configurations include angle diversity (spotlight), frequency diversity and multiple antenna systems.

20 DISTRIBUTION/AVAILABILITY OF ABSTRACT	21 ABSTRACT SECURITY CLASSIFICATION	
☒ UNCLASSIFIED/UNLIMITED ☐ SAME AS RPT ☐ OTIC USERS		
22a. NAME OF RESPONSIBLE INDIVIDUAL David R. Lyzenga	22b TELEPHONE (Include Area Code) (313)994-1200	22c. OFFICE SYMBOL

DD FORM 1473, 84 MAR
U.S. Government Printing Office: 1985—507-047

SECURITY CLASSIFICATION OF THIS PAGE
Unclassified

TABLE OF CONTENTS

LIST OF FIGURES

1
INTRODUCTION

Numerous investigations have been carried out during the past decade into the application of synthetic aperture radar (SAR) technology to various oceanographic measurement and detection problems. These investigations utilized the Seasat SAR and several aircraft-mounted SAR systems, which differ in many details but are all representative of the same general type of system, i.e., the conventional strip-map SAR which is described in Section 2 of this report. The results of these investigations indicate that strip-map SAR systems can provide useful information on a variety of phenomena including surface gravity waves, internal waves, bottom topographic features, ocean currents, fronts, winds, surface films, and sea ice. However, these systems are also subject to certain limitations and restrictions. These include operation at a fixed look direction and a single transmitted wavelength. In an attempt to relieve these limitations, several modifications of the conventional SAR system design have been proposed in recent years, some of which have been implemented and some of which are still conjectural. These advanced SAR concepts are described, and their possible advantages for ocean remote sensing are discussed in Section 3 of this report.

In order to evaluate the utility of SAR for measuring surface gravity wave spectra, as well as for other ocean applications, a numerical image simulation model has been developed and tested using SIR-B data. This model is described in Appendix A of this report. Additionally, efforts have been made in collaboration with F. Monaldo of the Applied Physics Laboratory to develop procedures for estimating wave height and slope spectra from SAR images. A published report on the results of this collaboration are reproduced in Appendix B of this document.

2
CONVENTIONAL SAR SYSTEMS

The conventional type of SAR system, which includes Seasat, SIR-A, and SIR-B as well as several different aircraft SAR systems, consists of a transmitter which generates a sequence of microwave pulses, an antenna which is maintained in a fixed orientation relative to the flight direction, a receiver which measures and records the amplitude and phase of the returned signals, and a processing system which reconstructs the recorded signals into a map or image of the scene. This type of system is commonly referred to as strip-map SAR. A diagram of the data collection geometry for this type of system is shown in Figure 1.

The transmitted pulses are usually in the form of linear FM signals which are converted into equivalent short pulses by convolving the returned signal with a reference signal having a form similar to that of the transmitted pulse. In this way, a high spatial resolution in the cross-track or range direction is obtained. The range resolution in this type of system is given by

$$\rho_r = \frac{c}{2B_r} \tag{1}$$

where c is the speed of light and B_r is the bandwidth of the transmitted signal.

In the along-track or azimuth direction, a similar method is used except that the frequency modulation is obtained from the Doppler shift of the reflected signals due to the platform motion. The azimuth resolution is given by

$$\rho_a = \frac{V}{B_a} \tag{2}$$

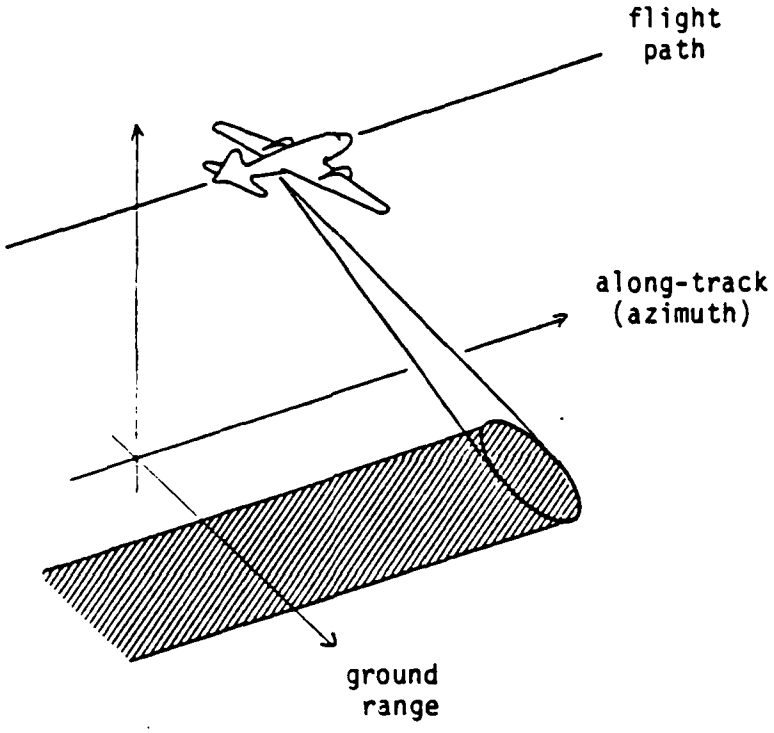

Figure 1. Strip-Map SAR Data Collection Geometry

where V is the platform velocity and B_a is the azimuth bandwidth, which is related to the antenna beamwidth β, the platform velocity V, and the radar wavelength λ by the equation

$$B_a = \frac{2\beta V}{\lambda} . \tag{3}$$

Since the antenna beamwidth is given by the ratio of the radar wavelength to the antenna length, the azimuth resolution is nominally equal to half the antenna length [1].

In actuality, Eq. (2) represents a limiting value for the resolution, which is not attained if there are phase errors due to scatterer motions or variations in the platform velocity. Nevertheless, the azimuth resolution of a SAR is improved (within limits) by broadening the antenna beam rather than by narrowing it as in a real aperture radar system. Also, the azimuth resolution is independent of range instead of being proportional to range as in a real aperture system. Thus, the synthetic aperture technique allows fine resolution imagery to be obtained from high altitudes. For example, to obtain the same resolution as the Seasat SAR with a real aperture radar at the same altitude and wavelength would require an antenna more than 15 km long.

The increased resolution obtainable by synthetic aperture techniques is obtained at the cost of a larger amount of processing than is required for real aperture radars. Usually, this processing is carried out as a separate stage, after the data collection is completed. However, developments in digital processing technology have made real-time on-board processing feasible, and SAR systems utilizing such processors now exist [2]. Research is continuing in the development of more efficient processors as well as algorithms for the extraction of specialized information from SAR data [3].

Because the azimuth resolution in a SAR is obtained by utilizing the Doppler shift of the returned signal as the object passes through the antenna beam, the imaging process is influenced by the motion of

the objects imaged. An object having a constant velocity V_r in the line of sight direction is displaced in the image by an amount

$$\Delta x = \frac{R}{V} V_r \tag{4}$$

in the along-track direction, where R is the radar range and V is the platform velocity. If the object changes its radial velocity (i.e., accelerates) during the time it is within the antenna beam, its image is smeared in the along-track direction by an amount proportional to the change in its radial velocity during this time.

In the case of the ocean surface, the image displacements caused by the motion of the surface can cause variations in the image intensity which may either enhance or degrade the visibility of surface features such as gravity waves or current boundaries. The orbital motions associated with gravity waves can cause these waves to be imaged by a SAR because of the differential displacement (or velocity bunching) effect, even when the waves would not be imaged by a real aperture radar system [4]. The effects of scatterer accelerations and random motions, on the other hand, cause a degradation in the azimuth resolution which may smear out a pattern which would otherwise be resolvable [5].

The following paragraphs summarize the current status of investigations into the use of SAR for various oceanographic applications. This summary is not comprehensive, but is intended to give an overview of this field of research as well as some recent results.

2.1 SURFACE GRAVITY WAVES

The oceanographic application of SAR which has received perhaps the most attention to date is the measurement of surface gravity wavelengths and directions. A number of field experiments dedicated to this problem were conducted during the 1970's, including the 1975 Marineland experiment [6], several experiments held during the Seasat

mission [7, 8], and the 1979 MARSEN experiment [9]. More recent experiments such as those conducted during the SIR-B mission [10] have also addressed this problem using a wider range of wave conditions, different sensor parameters, and more accurate in situ measurements.

The experiments conducted to date have demonstrated that under certain environmental conditions and SAR system configurations, the dominant wavelength and direction can be accurately estimated from SAR data. The precise range of conditions under which these quantities are measurable is a complicated function of the SAR system as well as environmental parameters, and has not yet been completely defined. However, in general waves which are traveling in the range direction (see Figure 1) are more easily detected and more accurately measured than those traveling in the along-track direction [11-12].

An example is provided by the Marineland SAR data set which was collected with eight different look directions on successive overflights. Figure 2 shows the X- and L-band images from three of these passes, for which the look direction was approximately cross-wave (upper images), down-wave (middle) and up-wave (lower images). Visual examination of these images indicates that range-traveling waves are more easily discernible than azimuth-traveling waves. A quantitative measure of the wave contrast, or modulation depth (defined in [11]) also indicates this dependence, as shown in Figure 3. Furthermore, estimates of the dominant wavelength and direction obtained from each pass are more accurate for the range traveling cases than the azimuth-traveling cases, as shown in Figures 4 and 5 (taken from Ref. [12]).

In addition to the experimental studies mentioned above, a great deal of theoretical work has been carried out regarding the mechanism by which SAR images gravity waves, in order to predict the range of detectability of these waves and the accuracy of their measurement by SAR. Numerous papers have been written on this subject, and an aura of controversy has surrounded the problem. A recent review and reformulation of this problem by Hasselmann, et al. [13] reflects the

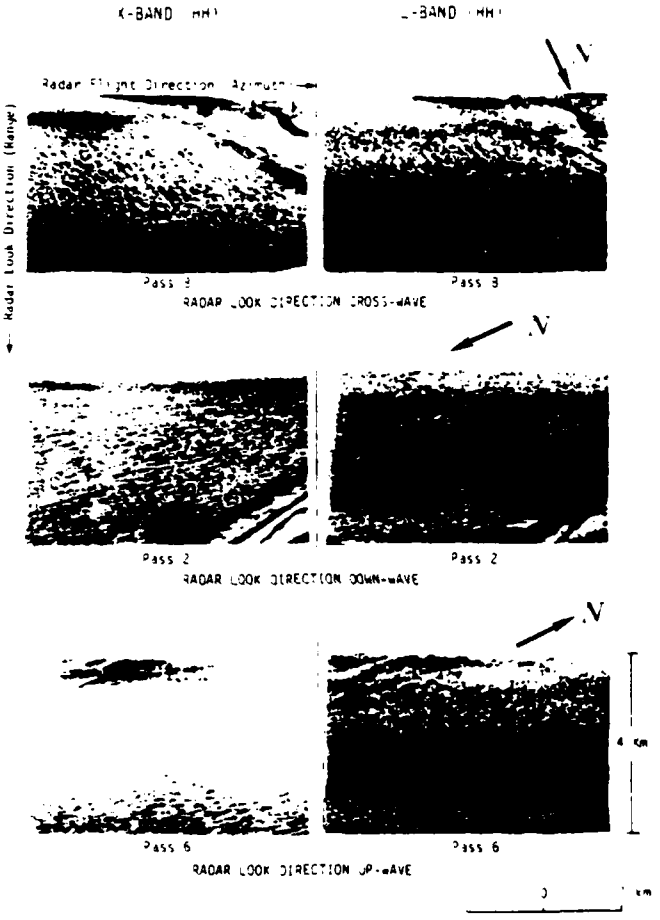

Figure 2. X- and L-Band SAR Data Collected During Marineland Experiment on 15 December 1975

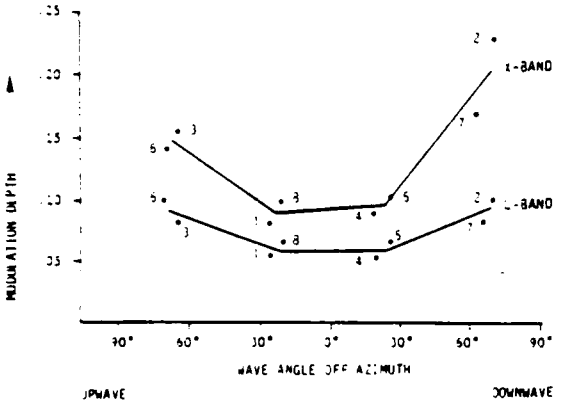

Figure 3. Modulation Depth Versus SAR Look Direction for Marineland Data Set [11]

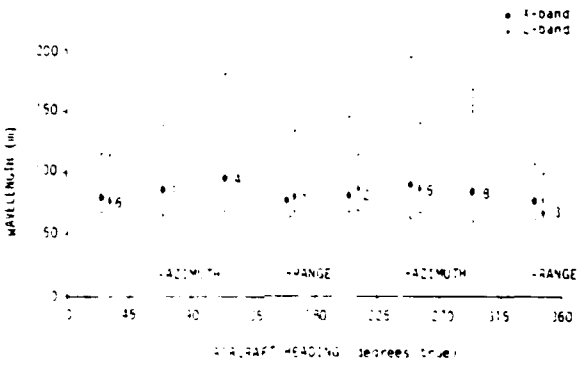

Figure 4. Apparent (SAR-Derived) Wavelength Versus SAR Look Direction for Marineland Data Set [12]

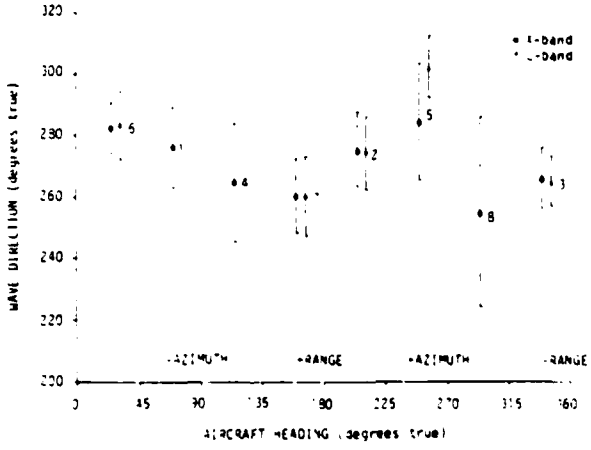

Figure 5. Apparent (SAR-Derived) Wave Direction Versus SAR Look Direction for Marineland Data Set [12]

opinions of many investigators although there is still disagreement regarding fundamental issues as well as the details of the imaging process [14, 15].

Because of the complexity of the SAR imaging process as well as the surface description, numerical simulation models have been found to be useful for understanding and predicting the SAR response to gravity waves [16, 17]. In the simulation model implemented at ERIM, the surface is assumed to be described by a wave height spectrum with statistically independent spectral components. A particular realization of the surface consistent with this description is computed by assigning random phases to each spectral component. The radar cross section of the surface is computed for each resolution cell using a modulation transfer function which incorporates both hydrodynamic and tilt effects [4], and the surface motion effects are included by computing the relevant motion parameters for each resolution cell [17].

Example results of this simulation procedure are shown in Figure 6. These images represent the predicted response of the Seasat and SIR-B systems to the wave height spectrum shown in Figure 7, which has a significant wave height of 3.6 meters and a dominant wavelength of 250 meters. The direction of the waves for the three cases shown in Figure 6 are 0^{o}, 45^{o} and 90^{o} with respect to the radar look direction. The results for Seasat confirm the experimental findings that gravity waves are more sensitively detected and more accurately represented on SAR images for which the look direction is nearly parallel to the wave propagation direction, than on those for which the look direction is at a large angle to the wave propagation direction. In particular, the apparent wave direction on the Seasat image for the 45^{o} case is shown in Figure 8 to deviate toward the range direction from the actual wave direction, by approximately 30^{o} for this case.

The results for SIR-B show that the SAR images and spectra (Figure 9) much more accurately represent the actual wave conditions than the Seasat images. The difference is due to the fact that the

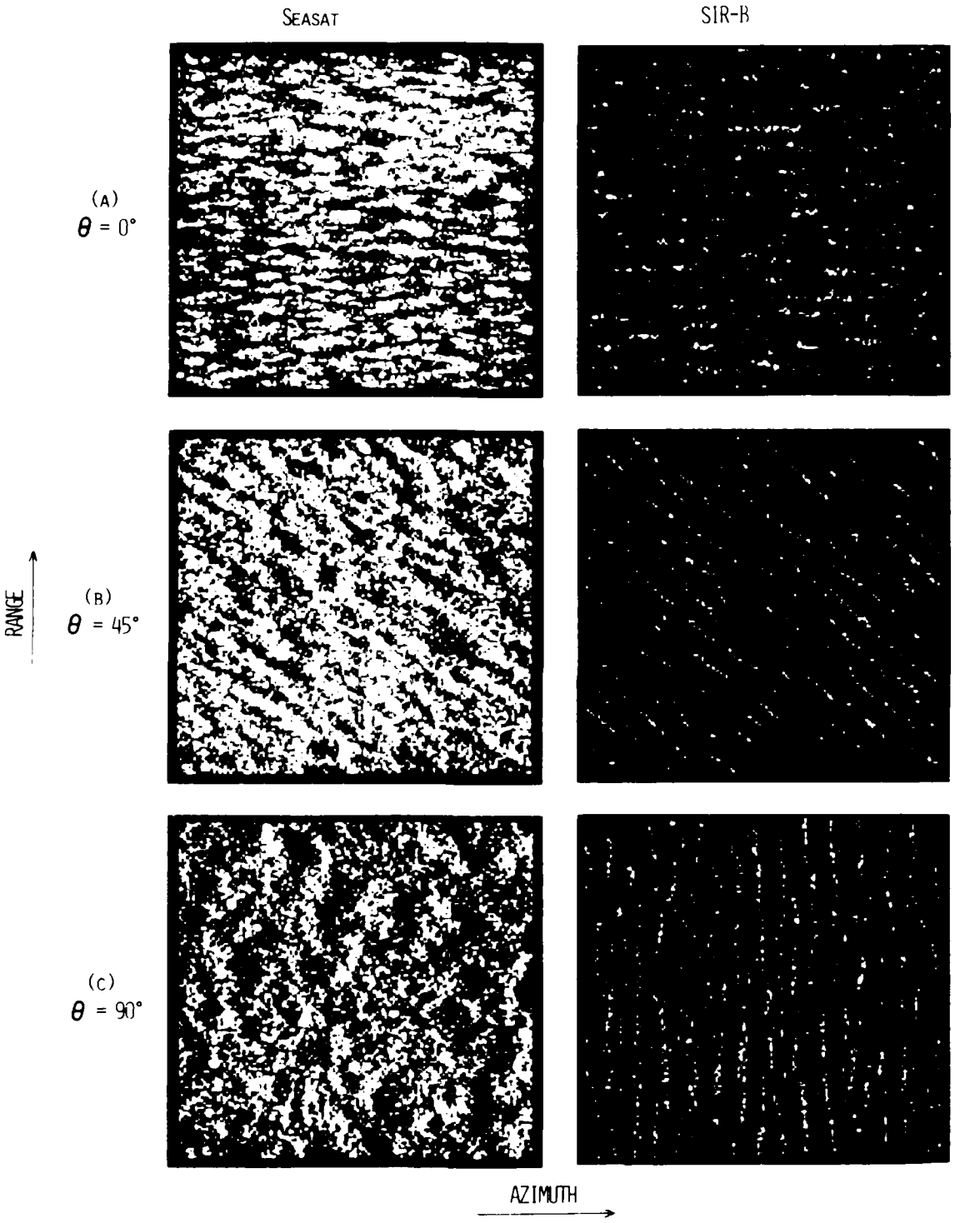

Figure 6. Seasat and SIR-B Simulations for Wave Conditions Described By Spectrum Shown in Figure 7, for Three Look Directions

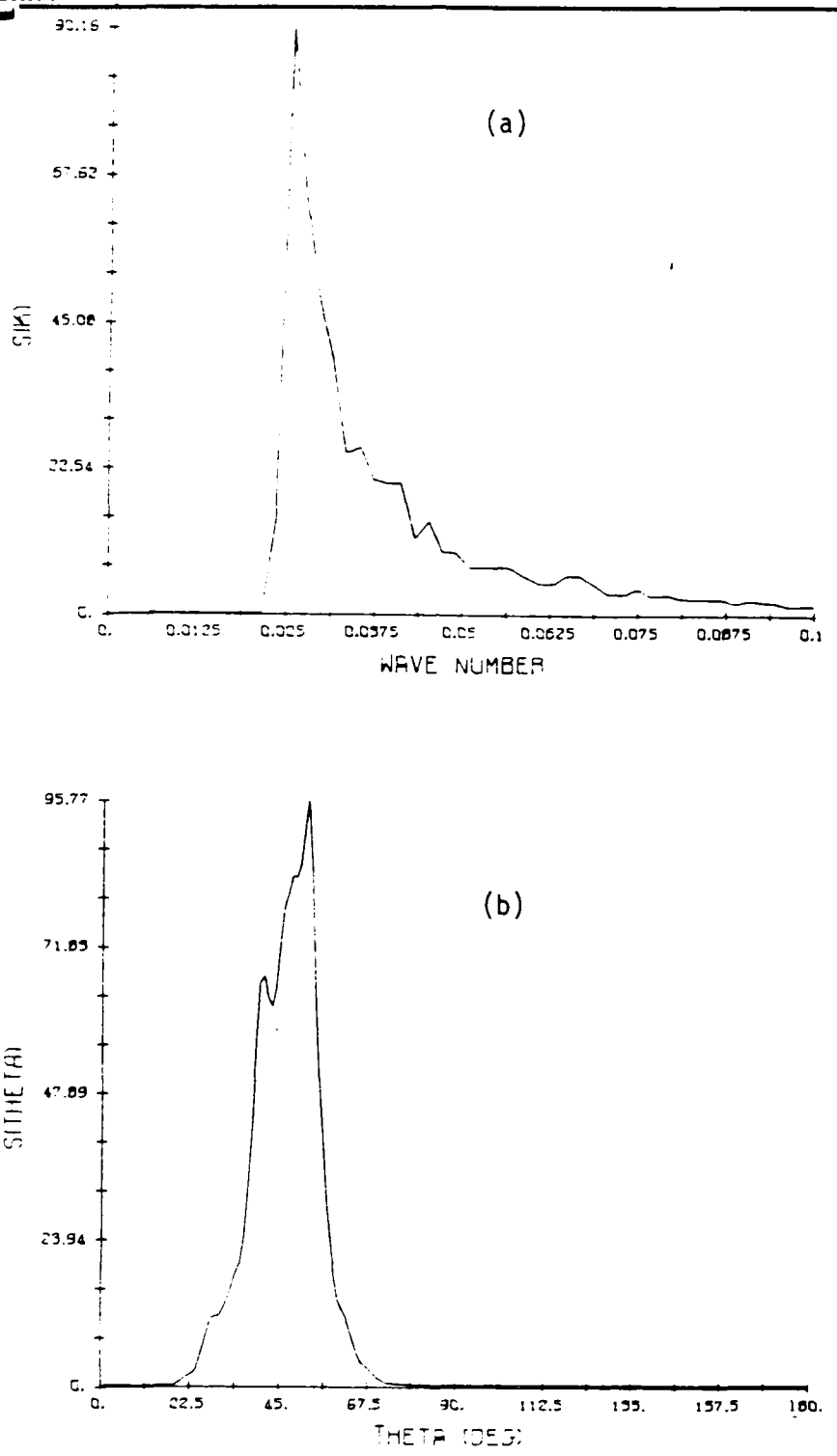

Figure 7. Wave Height Spectrum Used in Simulations, Expressed as a Function of (a) Wave Number, and (b) Wave Direction

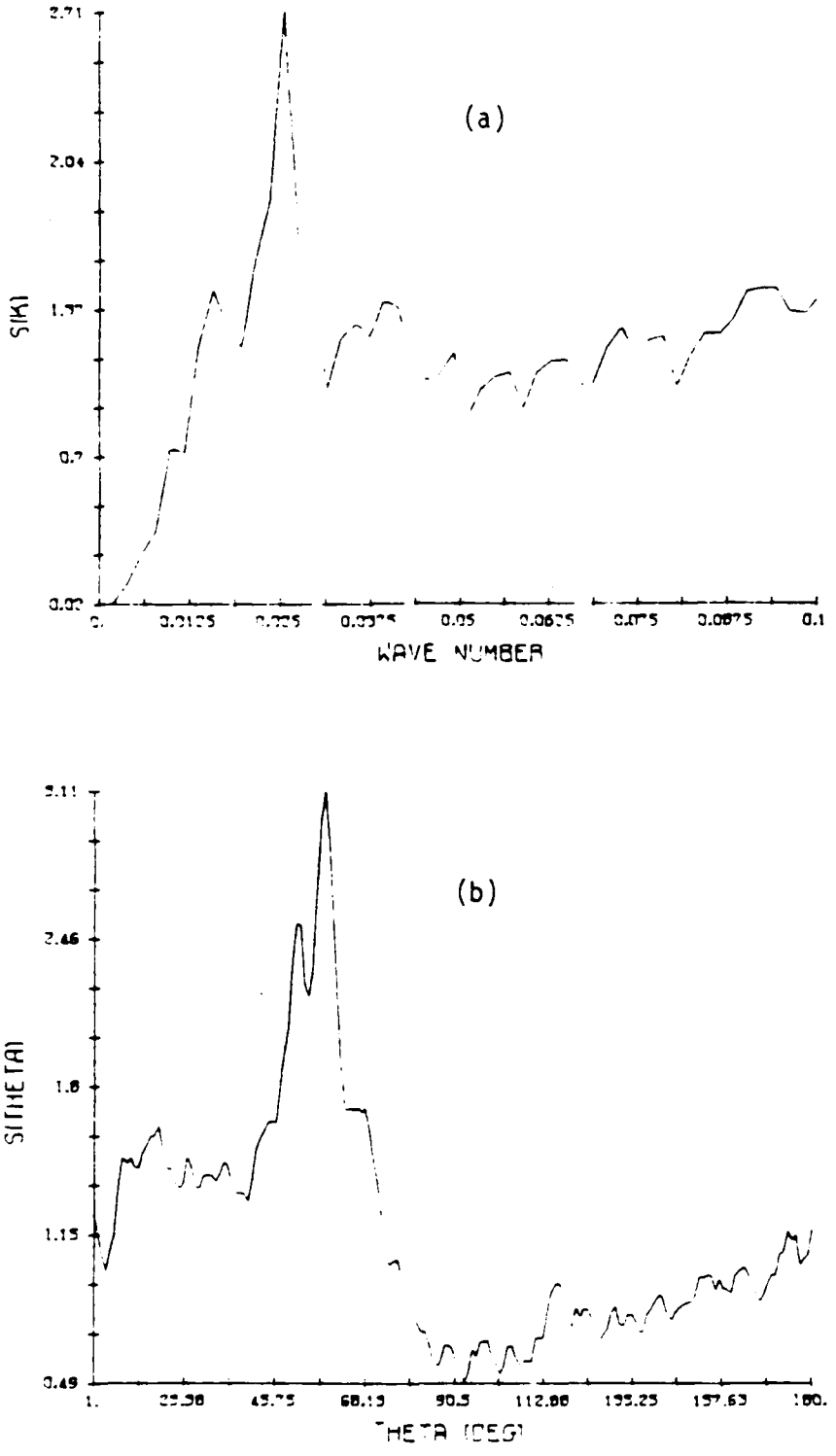

Figure 8. Seasat Image Spectrum for 45° Look Direction, Reduced to 1-D Spectra in Wave Number and Angle

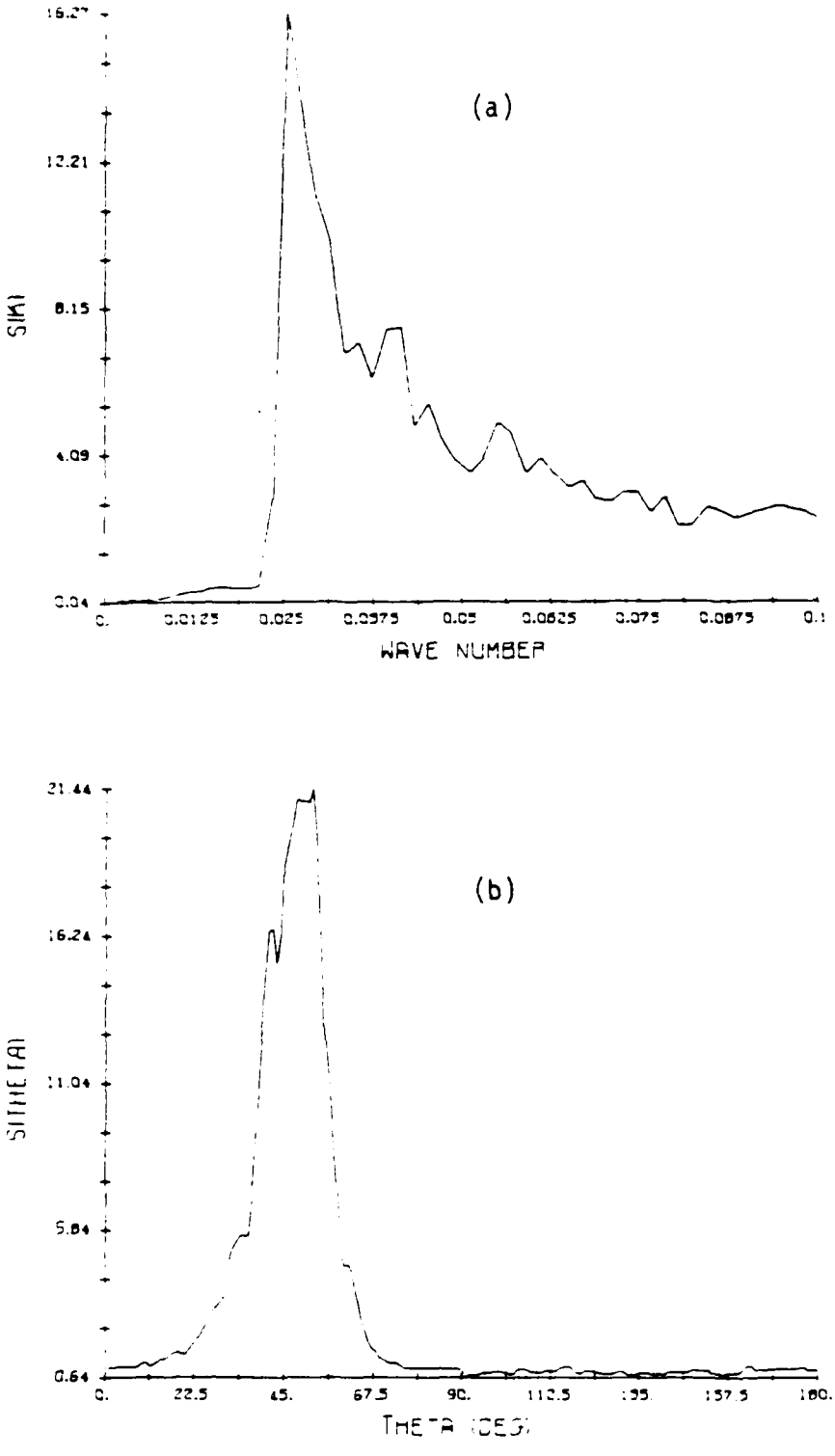

Figure 9. SIR-B Image Spectrum for 45^{o} Look Angle Reduced to 1-D Spectra as in Figure 8.

R/V ratio [see Eq. (4)] is equal to approximately 120 sec for Seasat and 35 sec for SIR-B. Thus, the degradation in image quality due to scatterer motions is much less severe for SIR-B than Seasat. These results have been confirmed by analyzing the data collected during the SIR-B mission [10, 17].

The implication of these results is that the look-direction limitations inherent in strip-map SAR systems can be at least partially obviated by the use of platforms with smaller R/V ratios. Another possible solution to this problem is the use of angle diversity or spotlight SAR systems which allow the look direction to be varied from the fixed (broadside) direction used in strip-map SARs. This concept is further explored in Section 3 of this report.

2.2 INTERNAL WAVES

Oceanic internal waves have been observed on both aircraft and Seasat SAR images [18-20] and have recently been the subject of several dedicated field experiments [21, 22]. The principal mechanism responsible for the imaging of internal waves by SAR is thought to be the interaction of short surface waves with the internal wave-induced surface currents. However, the damping effects of surface films, which are alternately compacted and dissipated by the internal wave surface currents, may also be a factor. Model calculations based on the former mechanism appear to slightly underpredict the observed features at L-band and to grossly underpredict the patterns observed on X-band imagery.

Although further research appears to be needed to quantitatively understand the contrast of the observed internal wave features (particularly at X-band), the existence and form of these features provide useful oceanographic information about the generation and propagation of internal waves. The presence of these features also yields information on stratification conditions and possibly on bottom topographic features which cause the internal waves to be formed.

The primary limitation of strip-map SAR systems for observing internal waves is their sensitivity to look direction. The scattering of microwave radiation from the surface is controlled primarily by the amplitude, or spectral density, of waves traveling in the range direction and having wavelengths which satisfy the Bragg criterion, i.e.,

$$\lambda_B = \lambda_o/(2 \sin \theta) \tag{5}$$

where λ_o is the radar wavelength and θ is the incidence angle. These waves interact with the surface currents induced by internal waves, and the resulting variations in their amplitude or spectral density cause variations in the surface reflectivity, which are detected by the SAR. The strength of the wave-current interaction is highly dependent on the relative angle between the current direction and the Bragg wave propagation direction (or radar look direction). In particular, internal waves propagating perpendicularly to the line of sight direction cause smaller changes in the Bragg wave amplitude, and therefore are less detectable, than those traveling in the line-of-sight direction.

In the conventional strip-map SAR configuration, the look direction is always normal to the ground track. As a result, internal waves traveling parallel to the ground track are less detectable than those traveling perpendicularly to the ground track. Angle diversity techniques remove this limitation by allowing the look direction to be varied (in spotlight mode) or by using two or more fixed look directions (in squint mode), for example at angles of ±45 to the normal broadside viewing direction.

Additionally, since the strength of the wave-current interaction depends on the wavelength of the surface waves, the detectability of internal waves may be optimized by using the frequency diversity techniques discussed in Section 3.2. These may involve either changing the frequency of the transmitted signal, and thus varying the Bragg

wavelength, or using two closely-spaced frequencies. The latter technique effectively causes the system to respond to surface waves with wavelengths which are determined by the difference frequency [see Eq. (9)].

2.3 BOTTOM TOPOGRAPHY

Several types of features on SAR images can be used to make inferences regarding bottom topography [23]. These include internal wave patterns (as discussed in the previous section), surface gravity waves with wavelengths sufficiently long to interact with the bottom, and patterns associated with local variations in tidal currents due to the interaction of these currents with the bottom topography.

The latter type of bottom-related features show a striking amount of detail. Well-known examples include Seasat images of the English Channel and the Nantucket Shoals. Several modeling studies using an approach similar to that used in the modeling of internal wave signatures have been carried out [24-26]. These models yield generally good agreement with observed L-band SAR intensity modulations except for certain geometries which produce much larger modulations than predicted by the models.

Because of the relative success in modeling these features, there is some hope of developing an inversion technique to calculate water depths from the observed SAR signals. However, since these signatures are highly dependent on the wind conditions as well as the currents, a knowledge of the wind and current speeds and directions would be needed to carry out such an inversion.

The SAR signatures associated with bottom topography are also look-angle dependent and therefore could be optimized by the use of angle diversity techniques. The optimum look direction is in general parallel to the direction in which the gradient of the water depth is

a maximum. Effects of scatterer motions are not critical to the formation of these signatures, although the resolution degradation due to random surface motions may contribute to the look-angle dependence.

2.4 OCEAN CURRENTS

Current boundaries are frequently visible on SAR images, possibly because of variations in surface roughness as well as surface velocity across the boundary. Variations in surface roughness are manifested as a change in the image intensity (tone) across the boundary, while changes in the surface velocity manifest themselves through the Doppler shift effect [27]. These image patterns may be used to chart the position of large-scale current features such as the Gulf Stream.

A quantitative measurement of the surface current speed may also be possible by performing a spectral analysis of the recorded SAR signals or the complex SAR image [28, 29]. The Doppler spectrum of these signals is determined by the antenna pattern, the platform velocity and the radar wavelength. For stationary surfaces, the maximum spectral density occurs at zero frequency, assuming the antenna is aligned perpendicularly to the flight path. If the entire surface within the field of view of the antenna is moving with a radial velocity V_r, the Doppler spectrum is shifted by an amount

$$\Delta f = \frac{2V_r}{\lambda} \tag{6}$$

where λ is the radar wavelength. If this shift is an appreciable fraction of the Doppler bandwidth B_a, given in Eq. (3) above, and if the antenna pointing angle remains stable, the shift can be measured and used to infer the radial component of the surface velocity. Measurements of surface currents in the range of 1-2 m/s have been measured using aircraft X-band SAR data in this way [30, 31].

Attempts to apply this method to Seasat data have not been successful because the Doppler bandwidth due to the platform motion is

too large compared to the Doppler shifts induced by surface currents. The Doppler bandwidth can be reduced by narrowing the antenna beamwidth, as shown by Eq. (3), but this implies a degradation in azimuth resolution, for a given radar wavelength. Comparison of Eqs. (2), (3) and (6) shows that for $\Delta f/B_a$ to be on the order of 0.1, while maintaining a resolution ρ_a, the radar wavelength must be on the order of

$$\lambda \sim 20\rho_a V_r/V \tag{7}$$

in order to measure a radial velocity V_r. This analysis indicates that an X-band SAR having the same resolution as Seasat and operating at the same altitude should be marginally able to detect a radial velocity of 1 m/s. Measurements of smaller currents would require a narrower antenna beam and consequently a coarser azimuth resolution.

An alternative method of measuring surface currents using multiple-antenna SAR systems is suggested in Section 3.3. This method could also be combined with angle diversity methods to measure both components of the current.

2.5 WINDS

Since the radar cross section of the ocean surface is dependent on the wind speed, it is possible to determine the wind speed and direction by a series of radar cross section measurements taken with different look directions [32]. The same principle allows an estimate of wind speed to be made from the average image intensity within a SAR image [33] although the wind direction cannot be determined by this method since only one look direction is usually employed. Again, angle diversity methods offer the possibility of overcoming this limitation.

A second method of obtaining wind information from SAR images is to examine the imagery for the existence of wind rows, or roll vortices [34]. These features can be quantified by doing a spectral analysis of the image, and the results used to estimate the wind speed and

direction. The spacing of the rows is related to the wind speed and their orientation may be used to infer the wind direction [35]. These features also appear to be look angle dependent and would benefit from the use of multiple look directions.

3
NON-CONVENTIONAL SAR SYSTEMS

Several variations on the conventional SAR system design have been either proposed or constructed in recent years [36]. These non-conventional systems are described, and their potential applicability to oceanographic measurement problems are discussed in the following sections.

3.1 ANGLE DIVERSITY TECHNIQUES

The along-track resolution of a SAR is determined by the Doppler bandwidth of the signals, which is in turn determined by the range of angles over which a given object is illuminated. In a conventional or strip-map SAR, this range of angles is equal to the antenna beamwidth, since the antenna is held in a fixed orientation perpendicular to the flight direction. Several alternative modes of operation, referred to collectively as angle diversity techniques, have been devised in which the antenna is not held in this fixed orientation.

In one of these modes, referred to as spotlight mode, the antenna is continuously rotated so as to illuminate a given area on the surface. Other variations include squint mode, in which the antenna is held in a fixed but arbitrary orientation, and swath mode, in which the antenna orientation is programmed to map out an arbitrary path on the surface. A diagram of the data collection geometry for these modes is shown in Figure 10.

In spotlight mode, the along-track resolution is controlled by the angle $\Delta\theta$ over which the antenna is rotated, and the scene size is determined by the antenna beamwidth. In order to achieve this resolution, however, a modified method of recording and processing the data is required. The polar format technique developed by Walker [37] makes the spotlight mode of operation feasible. This technique has been implemented optically by recording the time histories for each

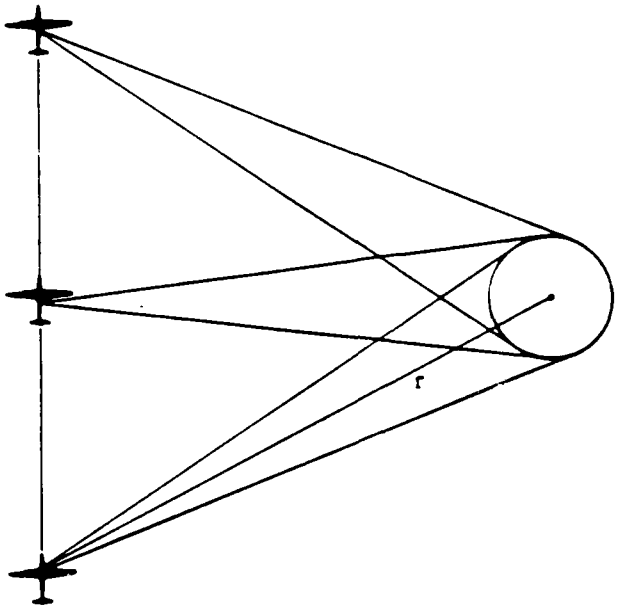

Figure 10. Angle Diversity (Spotlight) Viewing Geometry

returned pulse along a series of radial lines on a circular film, rather than along a series of parallel lines on a strip of film as is done in the conventional SAR case. In the digital implementation, the same result is obtained by a resampling procedure.

During processing, the entire data set can be processed coherently in order to maximize the resolution, or the data can be processed in segments at a coarser resolution in order to obtain a number of independent looks or images of the scenes. For a segment corresponding to an angular interval $\Delta\theta_i$, the azimuth resolution is given by

$$\rho_a = \frac{\lambda}{2\Delta\theta_i} \tag{8}$$

where λ is the radar wavelength. If N such angle intervals are processed and incoherently summed, the signal variance due to speckle on a distributed scene is reduced by a factor of 1/N over that for a fully coherent, or single-look image.

Other methods of processing, or information extraction, may be beneficial if the scene imaged is either time-dependent or aspect-angle dependent. These methods would make use of the fact that data can be collected by angle diversity systems over an extended time interval (a few seconds to a few tens of seconds) as well as an extended angular interval. For example, gravity wave images collected over an extended period of time could be used to obtain independent spectral estimates which can be averaged together to increase the number of degrees of freedom. Alternatively, images formed from each sub-interval could be compared with each other to look for differences, rather than summed together to reduce speckle.

Differences in time between sub-intervals might be used to quantify ice movements or surface currents, or to determine the direction of propagation of gravity waves and thus resolve the 180° ambiguity inherent in conventional SAR measurements of wave direction. Differences in look direction between sub-intervals could be used to

optimize the detectability of surface patterns which have a strong angle dependence, or to classify surface features on the basis of this dependence. Similar advantages may apply to squint mode systems, particularly those employing multiple antennas, as described in Section 3.3 of this report.

3.2 FREQUENCY DIVERSITY TECHNIQUES

Another category of advanced SAR system concepts concerns the utilization of multiple radar frequencies or frequency intervals. One type of multi-frequency SAR is that which collects data simultaneously but not coherently at two or more widely separated wave-lengths. An example of an existing SAR system of this type is the ERIM/CCRS X-L-C band SAR, which collects data simultaneously at either X and L band or X and C band.

The advantage of this type of system is that it allows information about ocean processes and scattering phenomena to be inferred from the wavelength dependence of the signals. For example, the interaction of short gravity and capillary waves with surface current gradients, such as those caused by internal waves or tidal currents flowing over bottom topographic features, results in patterns of reflectivity variations which are wavelength dependent. By comparing these patterns at different wavelengths, a better understanding of the hydrodynamic interactions involved can be gained, and these wave-length differences may eventually be used to extract more detailed oceanographic information from the images. Full exploitation of these possibilities requires radiometric calibration of the SAR data, techniques for which are currently being developed [38].

A second type of multi-frequency SAR utilizes the interference between the surface returns at two closely spaced frequencies in order to gain information about the surface structure on a spatial scale which is related to the difference frequency (Δf). The output signal

from such a SAR system is proportional to the surface reflectivity spectral density at the surface wavelength

$$\lambda_s = \frac{c}{2(\Delta f) \sin \theta} \tag{9}$$

where θ is the incidence angle and c is the speed of light. The principal oceanographic application of this type of system would be the measurement of spectral perturbations for surface wavelengths not resolvable by conventional SAR systems. Such a measurement capability might be useful for the detection of features such as internal waves which cause large perturbations of waves within a relatively narrow spectral region due to resonant interactions, wave trapping or blocking.

Preliminary studies have indicated the feasibility of such systems by segmenting the range bandwidth of a conventional SAR system into two narrow intervals with a variable spacing. When this spacing was set to correspond to the wavelength of a known surface feature, according to Eq. (9), the output of this simulated Δf system was observed to be a maximum. The range of observable wavelengths in this demonstration was limited by the signal bandwidth to values larger than the SAR resolution. However, a specially designed system incorporating a larger frequency difference could remove this restriction and produce more useful results.

3.3 MULTIPLE ANTENNA SYSTEMS

The final type of advanced SAR system considered in this report is that which incorporates multiple antennas, mounted on the same platform but displaced in either the along-track or across-track directions, or mounted on different platforms. The purpose of these arrangements is to measure special attributes of the scene in addition to its reflectivity, such as the surface elevation or roughness, or the motion of the surface or of objects within the scene.

A two-antenna SAR system for measuring target motions was proposed by Raney [39] using a phase detection method. In this scheme, coherent pulses are transmitted through two antennas separated in the along-track direction by a distance D, with the pulse fed to the second antenna delayed by an amount

$$\delta t = D/V \tag{10}$$

where V is the platform velocity. Thus, the two pulses are transmitted and received at exactly the same locations relative to the scene. If the scene were stationary, therefore, the difference between the received signals would be zero, whereas if a given scatterer has a radial velocity V_r, the received signals would differ by a phase

$$\Delta\phi = 2kV_r\delta t \tag{11}$$

where k is the radar wavenumber, and the magnitude of the difference signal would be

$$\frac{\delta s}{|s|} = 2 \sin (kV_r\delta t) \tag{12}$$

where |s| is the magnitude of the total signal received from the scatterer. By appropriately choosing the antenna separation D, any given range of velocities could thus be measured. For example, in order to measure a radial velocity on the order of 0.1 m/s from an earth-orbiting platform (V ~ 7 km/s) with an X-band system, an antenna separation on the order of 35 meters would be required.

A second method of observing the motions of persistent objects, such as sea ice, would be to operate a squint-mode SAR with two antennas having an angular separation $\Delta\theta$, so that the same area is imaged twice with a time difference

$$\Delta t \simeq (R/V)\Delta\theta \tag{13}$$

where R is the range distance and V is the platform velocity. If the target velocity is sufficient to cause a motion through several resolutions cells during this time interval, the velocity would be measurable by this method. For a squint-mode SAR operating at Seasat altitudes (R/V ~ 120 sec) with a resolution of 10 meters, an angular separation of 45_0 would allow velocities on the order of 0.5 m/s to be measured. The advantage of this method is that it allows both components of the velocity to be measured simultaneously.

The use of two or more antennas displaced in the across-track direction allows the possibility of measuring surface elevations or roughness. Basically, this is because two or more instantaneous measurements of range, plus a measurement of the along-track coordinate, allows each scatterer to be located in three dimensions. Several implementations of this concept have been attempted, including the hologram radar system developed at ERIM [40] and the synthetic interferometer radar developed at Goodyear Corp. [41]. The former system used an array of 100 receiving antennas arranged in the across- track direction, the signals from which were coherently recorded and processed to yield an output image. Resolution in the along-track direction is obtained by the synthetic aperture technique. By transmitting two closely-spaced frequencies, a range contouring capability was demonstrated over terrestrial scenes. A modification of this design could conceivably yield useful oceanographic information such as wave heights or surface roughness.

The Goodyear system [41] uses two antennas mounted vertically to obtain two independent range measurements, and also utilizes the synthetic aperture technique to obtain azimuth resolution. Summing the signals coherently from the two antennas results in a set of fringes or nulls at fixed depression angles. The location of these nulls in the output imagery gives information on both the range and the depression angle, which allows the surface elevation to be computed with a

known ambiguity factor. This concept was also demonstrated over terrestrial scenes and may conceivably be modified or generalized to yield oceanographic information.

The term bistatic SAR might be applied to any of the multiple antenna systems described above, but is usually reserved for the case where the transmit and receive antennas are located on different platforms and the antenna separation is therefore much larger. Previous discussions of bistatic SAR have emphasized the possible operational advantages of such systems for real-time and continuous monitoring applications [42]. It would appear that additional surface elevation or topographic information could be obtained by a comparison of simultaneous monostatic and bistatic images of the same area, since each contains an independent measurement of the range distance to each target.

4
SUMMARY

Strip-map SAR systems are useful for observing a variety of oceanic phenomena, but are limited primarily by their sensitivity to the look direction of the SAR relative to the phenomenon being observed. This restriction is alleviated by the use of angle diversity SAR techniques which allow the look direction to be varied independently of the direction of motion of the SAR platform. These techniques may also prove to be useful for gaining information on scene motions or for classifying scene elements based on their look directional dependence. Additionally, angle diversity data of the oceans can be processed using non-coherent averaging or multiple-look techniques to reduce the effects of background noise. This background noise is multiplicative in nature and is a result of the coherent nature of the SAR. Under low to moderate winds, this system noise or speckle can dominate an image and in some cases mask subtle oceanography features of interest. This is a particularly acute problem in respect to detection of bottom topography.

Frequency diversity SAR systems utilizing multiple-wavelength transmissions may also increase the accuracy of detection and classification of surface patterns, based on the wavelength dependence of the surface reflectivity. Finally, the use of multiple antenna systems may offer the possibility of measuring surface motions at high resolution, or of providing continuous imaging with two or more look directions.

REFERENCES

1. W.M. Brown and L. Porcello, An Introduction to Synthetic Aperture Radar, IEEE Spectrum, 6, pp. 52-66, 1969.

2. A. Nichols, T. Gaffield, J. Wilhelm, R. Inkster, and S. Leung, A SAR for Real-Time Ice Reconnaissance, Proc. 1984 International Geoscience and Remote Sensing Symposium (IGARSS '84), Strasbourg, France, pp. 71-76, 1984.

3. I.J. LaHaie, A.R. Dias, and G.D. Darling, Digital Processing Considerations for Extraction of Ocean Wave Image Spectra from Raw Synthetic Aperture Radar Data, IEEE Journal of Oceanic Eng., OE-9, 114-120, 1984.

4. W.E. Alpers, D.B. Ross, and C.L. Rufenach, On the Detectability of Ocean Surface Waves by Real and Synthetic Aperture Radar, J. Geophys. Res., 86, 6481-6498, 1981.

5. R.K. Raney, Wave Orbital Velocity, Fade, and SAR Response to Azimuth Waves, IEEE J. Oceanic Eng., OE-6, 4, 1981.

6. W. McLeish, D.B. Ross, R.A. Shuchman, P.G. Teleki, S.V. Hsiao, O.H. Shemdin, and W.E. Brown, Synthetic Aperture Radar Imaging of Ocean Waves: Comparison with Wave Measurements, J. Geophys. Res., 85, pp. 5003-5011, 1980.

7. F.I. Gonzalez, R.C. Beal, W.E. Brown, P.S. DeLeonibus, J.W. Sherman, J.F.R. Gower, D. Lichy, D.B. Ross, C.L. Rufenach, and R.A. Shuchman, Seasat Synthetic Aperture Radar: Ocean Wave Detection Capabilities, Science, 204, pp. 1418-1421, 1979.

8. T.D. Allen and T.H. Guymer, Seasat and JASIN, Int. J. Remote Sensing, 1, pp. 261-267, 1980.

9. R.A. Shuchman, W. Rosenthal, J.D. Lyden, D.R. Lyzenga, E.S. Kasischke, H. Gunther, and H. Linne, Analysis of MARSEN X-Band SAR Ocean Wave Data, J. Geophys. Res., 88, pp. 9757-9769, 1983.

10. R.C. Beal, F.M. Monaldo, D.G. Tilley, D.E. Irvine, E.J. Walsh, F.C. Jackson, D.W. Hancock III, D.E. Hines, R.N. Swift, F.I. Gonzalez, D.R. Lyzenga, and L.F. Zambresky, A Comparison of SIR-B Directional Ocean Wave Spectra with Aircraft Scanning Radar Spectra, Science 232, pp. 1531-1535, 1986.

11. R.A. Shuchman and O.M. Shemdin, Synthetic Aperture Radar Imaging of Ocean Waves during the Marineland Experiment, IEEE J. Oceanic Eng., OE-8, pp. 83-90, 1983.

12. R.A. Shuchman, J.D. Lyden, and D.R. Lyzenga, Estimates of Ocean Wavelength and Direction from X- and L-band Synthetic Aperture Radar Data Collected During the Marineland Experiment, IEEE J. Oceanic Eng., OE-8, pp. 90-96, 1983.

13. K. Hasselmann, R.K. Raney, W.J. Plant, W. Alpers, R.A. Shuchman, D.R. Lyzenga, C.L. Rufenach and M.J. Tucker, Theory of SAR Ocean Wave Imaging: A MARSEN View, J. Geophys. Res., (in press) 1985.

14. R.O. Harger, A Fundamental Model and Efficient Inference for SAR Ocean Imagery, IEEE J. Oceanic Eng. OE-9, 266-276, 1984.

15. A. Jain, SAR Imaging of Ocean Waves: Theory, IEEE J. Oceanic Eng. OE-6, 130-139, 1981.

16. W. Alpers, Monte Carlo Simulations for Studying the Relationships between Ocean Wave and Synthetic Aperture Radar Image Spectra, J. Geophys. Res. 88, pp. 1745-1760, 1983.

17. D.R. Lyzenga, Numerical Simulation of Synthetic Aperture Radar Image Spectra for Ocean Waves, IEEE Trans. Geoscience and Remote Sensing, GE-24, 863-871, 1986.

18. B.A. Hughes and J.F.R. Gower, SAR Imagery and Surface Truth Comparisons of Internal Waves in Georgia Strait, British Columbia, Canada, J. Geophys. Res., 88, pp. 1809-1824, 1983.

19. W. Alpers and E. Salusti, Scylla and Charybdis Observed from Space, J. Geophys. Res., 88, pp. 1800-1808, 1983.

20. R.P. Trask and M.G. Briscoe, Detection of Massachusetts Bay Internal Waves by the Synthetic Aperture Radar (SAR) on Seasat, J. Geophys. Res., 88, pp. 1789-1799, 1983.

21. B.A. Hughes, S.J. Hughes, and T.W. Dawson, Joint Can/US Ocean Wave Investigation Project: Objectives, Procedures, and Description of DREP Data for the Georgia Strait Experiment (July/August 1983), Tech. Memo. 84-7, Defense Research Establishment Pacific, September 1984.

22. R.S. Winokur, J.R. Apel and R.F. Gasparovic, SAR Internal Wave Signature Experiment, in The SIR-B Science Investigations Plan, NASA JPL Publication 84-3, 1984.

23. E.S. Kasischke, R.A. Shuchman, D.R. Lyzenga, and G.A. Meadows, Detection of Bottom Features on Seasat Synthetic Aperture Radar Imagery, Photogrametric Engineering and Remote Sensing, 49, pp. 1341-1353, 1983.

24. D.R. Lyzenga, R.A. Shuchman, E.S. Kasischke, and G.A. Meadows, Modeling of Bottom-Related Surface Patterns Imaged by Synthetic Aperture Radar, International Geoscience and Remote Sensing Symposium (IGARSS '83) Digest, pp. FA-6-7.1-7.10, 1983.

25. W. Alpers and I. Hennings, A Theory of the Imaging Mechamisms of Underwater Bottom Topography by Real and Synthetic Aperture Radar, J. Geophys. Res., 89, 10529-10546, 1984.

26. R.A. Shuchman, D.R. Lyzenga and G.A. Meadows, Synthetic Aperture Radar Imaging of Ocean Bottom Topography via Tidal Current Interactions: Theory and Observations, International Journal of Remote Sensing, 6, 1179-1200, 1985.

27. L.I. Moskowitz, The Feasibility of Ocean Current Mapping via Synthetic Aperture Radar Methods, Proc. Amer. Soc. of Photogrammetry Fall Convention, Part II, pp. 760-771, 1973.

28. D.R. Lyzenga, R.A. Shuchman, and C.L. Rufenach, Synthetic Aperture Radar Measurements of Ocean Surface Currents, Geophys. Res. Lett., 9, 747, 1982.

29. C.L. Rufenach, R.A. Shuchman, and D.R. Lyzenga, Interpretation of Synthetic Aperture Radar Measurements of Ocean Currents, J. Geophys. Res., 83, pp. 1867-1876, 1983.

30. R.A. Shuchman, C.L. Rufenach, F.I. Gonzalez, and A. Klooster, The Feasibility of Measurement of Ocean Surface Currents Using Synthetic Aperture Radar, Proc. Thirteenth Int. Symp. Remote Sens. Environ., Ann Arbor, MI, pp. 93-102, 1979.

31. F.I. Gonzalez, C.L. Rufenach, and R.A. Shuchman, Surface Current Detection Using SAR Data, Oceanography from Space, ed. by J.F.R. Gower, Plenum Press, New York, pp. 511-523, 1981.

32. W.L. Jones, L.C. Schroeder, and J.L. Mitchell, Aircraft Measurements of the Microwave Scattering Signature of the Ocean, IEEE J. of Oceanic Eng., OE-2, pp. 52-61, 1977.

33. J.D. Lyden, D.R. Lyzenga, R.A. Shuchman, and W.L. Jones, Measurement of Ocean Surface Winds by Seasat Synthetic Aperture Radar, 1983 International Geoscience and Remote Sensing Symposium (IGARSS '83) Digest, pp. TA-5-8.1-8.12, 1983.

34. M.A. LeMone, The Structure and Dynamics of Horizontal Roll Vortices in the Planetary Boundary Layer, J. Atmos. Sci., 30, pp. 1077-1091, 1973.

35. T.W. Gerling, R.C. Beal, and D.G. Tilley, The Information Content of Spaceborne SAR Ocean Image Spectra, Proc. IGARSS '84 Symposium, Strasbourg, France, pp. 307-314, 1984.

36. D.A. Ausherman, A. Kozma, J.L. Walker, H.M. Jones, and E.C. Poggio, Developments in Radar Imaging, IEEE Trans. Aerospace and Elect. Systems, AES-20, pp. 363-399, 1984.

37. J.L. Walker, Range-Doppler Imaging of Rotating Objects, IEEE Trans. Aerospace and Electronics Systems, AES-16, pp. 23-52, 1980.

38. R.W. Larson, and P.L. Jackson, SAR Calibration: A Technology Review, IEEE Trans. Geosci. Remote Sensing, (in press) 1985.

39. R.K. Raney, Synthetic Aperture Imaging Radar and Moving Targets, IEEE Trans. Aerospace Elect. Syst., AES-7, pp. 499-505, 1971.

40. R.W. Larson, E.L. Johansen, and J. Zelenka, Results Obtained from the University of Michigan Microwave Hologram Radar, Proc. Seventh International Symposium on Remote Sensing of Environment, 17-21 May 1971, pp. 809-841.

41. L.C. Graham, Synthetic Interferometry Radar for Topographic Mapping, IEEE Proceedings, 62, pp. 763-768, 1974.

42. C. Elachi, R. Goldstein, and D. Held, Spaceborne Bistatic Synthetic Aperture Imaging Radar, Proc. 1981 International Geoscience and Remote Sensing Symposium (IGARSS '81), pp. 944- 950, 1981.

APPENDIX A

Numerical Simulation of Synthetic Aperture Radar Image Spectra for Ocean Waves

DAVID R. LYZENGA

Abstract—**A numerical model for predicting the synthetic aperture radar (SAR) image of a moving ocean surface is described, and results are presented for two SIR-B data sets collected off the coast of Chile. Wave height spectra measured by the NASA radar ocean wave spectrometer (ROWS) were used as inputs to this model, and results are compared with actual SIR-B image spectra from orbits 91 and 106. Additional parametric variations are presented to illustrate the effects of nonlinearities in the imaging process.**

I. Introduction

THE PROCESSES involved in the imaging of surface gravity waves by synthetic aperture radar have been widely discussed and debated within the radio-oceanographic community. A number of studies have been carried out to investigate these processes experimentally [1]–[7] as well as theoretically [8]–[14]. However, because of the large number of independent variables which influence the imaging process, the experimental difficulties involved in making the appropriate surface measurements, and differences of opinion regarding the formulation of the theory, a clear picture of the limitations of SAR for measuring ocean waves has been slow to emerge.

In the present paper, a conceptually simple model for the SAR imaging process is discussed and the numerical implementation of this model is described. Predictions of the SAR image spectra for various environmental conditions and SAR system parameters are presented, and comparisons are made with measured image spectra obtained during the SIR-B experiment. Additional parametric variations are presented to illustrate behavior over a wider range of environmental and SAR system parameters, and the possibility of obtaining wave height or slope spectra from SAR images is discussed.

II. Model Description

The microwave scattering properties of the ocean surface, including the phase changes due to surface motions, may be described in terms of a complex reflectivity $\rho(x, y, t)$ where x is the along-track coordinate, y is the across-track (or range) coordinate, and t is time. The signal received by a synthetic aperture radar within a given range cell (assuming the signal has been resolved in range, and neglecting range resolution effects) may then be written as

$$s(y, t) = \int \rho(x, y, t)\, a_1(x - Vt)\, e^{-j2kr(x, y, t)}\, dx \quad (1)$$

where $a_1(x - Vt)$ represents the antenna gain pattern, k is the electromagnetic wavenumber, and $r(x, y, t)$ is the instantaneous range distance from the scattering element at (x, y) to the SAR platform, which is located at $x = Vt$, $y = 0$, and $z = A$. Assuming that the antenna pattern limits the illumination to an along-track distance interval that is much smaller than the range distance, this range distance may be approximated by

$$r(x, y, t) = R + \frac{(x - Vt)^2}{2R} \quad (2)$$

where $R^2 = y^2 + A^2$. The integrand in (1), which may be interpreted as the contribution of a surface element at (x, y) to the total received signal, can then be written as

$$s(x, y, t) = \rho(x, y, t)\, a_1(x - Vt)\, e^{-jk[(x - Vt)^2/R]}\, e^{-j2kR} \quad (3)$$

neglecting the constant-phase term e^{-j2kR} that is common to all the surface elements considered in the integration.

The complex image amplitude is obtained by convolving the recorded signal with the reference function $h(x')$, i.e.

$$i(x', y') = \int s(y', t)\, h(x' - Vt)\, dt \quad (4)$$

where the reference function has the form

$$h(x' - Vt) = a_2(x' - Vt)\, e^{jb[(x' - Vt)^2]} \quad (5)$$

in which $a_2(x' - Vt)$ is the amplitude weighting and b is the quadratic phase factor or focus parameter, which is normally chosen as

$$b = k/R \quad (6)$$

in order to cancel the quadratic time dependence in the phase of the recorded signal. If this is so chosen, the contribution of the surface element at (x, y) to the complex image amplitude at (x', y') may be written as

$$i(x, x', y') = \tilde{\rho}(x, y, \omega)\, e^{-jk[(x - x')^2/R]} \quad (7)$$

where $y = y'$ (neglecting range resolution effects) and

$$\tilde{\rho}(x, y, \omega) = \int \rho(x, y, t)\, a(x, x', t)\, e^{-j\omega t}\, dt \quad (8)$$

Manuscript received February 18, 1986, revised June 27, 1986. This work was supported by NASA Headquarters under Contract N00014-81-C-0692.

The author is with the Radar Science Laboratory, Environmental Research Institute of Michigan, Ann Arbor, MI 48107.

IEEE Log Number 8610611.

0196-2892/86/1100-0863$01.00

with

$$a(x, x', t) = a_1(x - Vt)\, a_2(x' - Vt) \tag{9}$$

and

$$\omega = 2kV(x - x')/R. \tag{10}$$

As discussed in Hasselmann *et al.* [14], $\tilde{\rho}(x, y, \omega)$ may be interpreted as the finite-resolution Fourier transform of the surface reflectivity, with the resolution being determined by the width of the weighting function $a(x, x', t)$. For stationary scenes, $\tilde{\rho}(x, y, \omega)$ is centered at $\omega = 0$ and has a width inversely proportional to the width of $a(x, x', t)$. For randomly moving surfaces, $\tilde{\rho}(x, y, \omega)$ may be considered as a random variable that has non-zero values over a range of frequencies determined by the surface motion and the radar wavelength, and that has frequency correlation statistics determined by $a(x, x', t)$.

If the surface reflectivity is assumed to be spatially uncorrelated, i.e.

$$\langle \rho(x, y, t)\, \rho^*(x', y', t') \rangle = \langle \rho(x, y, t)\, \rho^*(x', y', t') \rangle\, \delta(x - x')\, \delta(y - y') \tag{11}$$

where the brackets denote ensemble averaging [14], the expected value of the image intensity is given by

$$\langle I(x', y') \rangle = \left\langle \left| \int i(x, x', y')\, dx \right|^2 \right\rangle = \int f_D(x, y, 2kV(x - x')/R)\, dx \tag{12}$$

where $y = y'$ and

$$f_D(x, y, \omega) = \left\langle \left| \int \rho(x, y, t)\, a(x, x', t)\, e^{-j\omega t}\, dt \right|^2 \right\rangle \tag{13}$$

is the finite-resolution Doppler spectrum of the surface reflectivity.

The simulation procedure suggested by this model is therefore to compute the Doppler spectrum of the surface reflectivity at each grid cell in the scene, and then to map the radar cross section onto the image using the Doppler spectrum to control the mapping, as illustrated in Fig. 1. The Doppler spectrum is approximated by a Gaussian-like function (actually a polynomial form is used) with a center location ω_0 and a width σ_ω. The total area under the spectrum is equal to the radar cross section $\sigma_0(x, y)$.

The center frequency ω_0 and width σ_ω may be expressed in terms of the surface velocity as

$$\omega_0 = 2kV_r \tag{14}$$

and

$$\sigma_\omega = 2k\sigma_v \tag{15}$$

where V_r is the mean radial velocity of the surface and σ_v is the standard deviation of the radial velocities within a given resolution cell. These velocities, and the radar cross section, are computed from the wave height spectrum as follows.

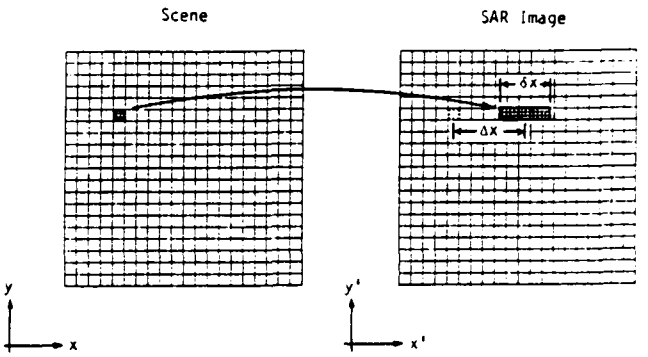

Fig. 1. Illustration of azimuthal shifting and smearing effects due to surface motions: $\Delta x = (R/V)\, V_r$ and $\delta x = 2(R/V)\, \sigma_v$, where V_r is the mean radial velocity and σ_v is the standard deviation of radial velocities within a given resolution cell.

Values of the wave height spectrum, or surface elevation spectral density, are assumed to be specified on a regular grid of spatial wavenumbers

$$k_m = \frac{2\pi}{L_x}(m - M/2), \qquad m = 1, \cdots, M - 1 \tag{16}$$

and

$$k_n = \frac{2\pi}{L_y}(n - N/2), \qquad n = 1, \cdots, N - 1 \tag{17}$$

where L_x and L_y are the dimensions of the scene in the along-track and across-track directions, respectively. Each of these wavenumbers is assumed to correspond to a freely propagating deep-water wave of amplitude a_{mn} and frequency

$$\omega_{mn} = (gk)^{1/2} \tag{18}$$

where g is the gravitational acceleration and k is the magnitude of the wavenumber. Thus, the surface elevation at time t, for a given realization of the spectrum, may be written as

$$z(x, y, t) = \sum_{m=1}^{M-1} \sum_{n=1}^{N-1} a_{mn} \cdot \cos(k_m x + k_n y - \omega_{mn} t + \Phi_{mn}) \tag{19}$$

where the phases Φ_{mn} are randomly selected from a uniform distribution over $(0, 2\pi)$. The amplitudes a_{mn} are proportional to the square root of the spectral density at (k_m, k_n), with the normalization chosen to produce the desired value for the significant wave height

$$H_s = 4\langle z^2 \rangle^{1/2} \tag{20}$$

where $\langle z^2 \rangle^{1/2}$ is the rms surface elevation.

The instantaneous radial velocity of the surface is computed as the sum of the orbital velocities of each compo-

nent, i.e.

$$V_r(x, y, t) = \sum_{m=1}^{M-1} \sum_{n=1}^{N-1} a_{mn}\omega_{mn}g_{mn} \cdot \cos [k_m x + k_n y - \omega_{mn}t + \Phi_{mn} + \Phi_v] \quad (21)$$

where

$$g_{mn} = [(k_n/k)^2 \sin^2 \theta + \cos^2 \theta]^{1/2} \quad (22)$$

$$\Phi_v = \tan^{-1}\left(\frac{k \cos \theta}{k_n \sin \theta}\right) \quad (23)$$

and θ is the incidence angle.

Assuming that scatterers are uniformly distributed over the water surface, the average radial velocity over each grid cell of dimensions Δx, Δy and over the integration time T is given by (21) with a_{mn} replaced by $a_{mn}b_{mn}$, where

$$b_{mn} = \frac{2}{k_m \Delta x} \sin\left(\frac{k_m \Delta x}{2}\right) \frac{2}{k_n \Delta y} \cdot \sin\left(\frac{k_n \Delta y}{2}\right) \frac{2}{\omega_{mn} T} \sin\left(\frac{\omega_{mn} T}{2}\right). \quad (24)$$

The radial velocity variance is calculated as the sum of the contributions from each resolved wave component plus the variance due to the subresolution-scale waves, i.e.

$$\sigma_v^2(x, y, t) = \sigma_{vs}^2 + \frac{1}{2} \sum_{m=1}^{M-1} \sum_{n=1}^{N-1} a_{mn}^2 \omega_{mn}^2 g_{mn}^2 \cdot [1 - c_{mn} + 2(c_{mn} - b_{mn}^2) \cdot \cos^2 (k_m x + k_n y - \omega_{mn}t + \Phi_{mn} + \Phi_v)] \quad (25)$$

where

$$c_{mn} = \frac{\sin (k_m \Delta x)}{k_m \Delta x} \frac{\sin (k_n \Delta y)}{k_n \Delta y} \frac{\sin (\omega_{mn} T)}{\omega_{mn} T} \quad (26)$$

and

$$\sigma_{vs}^2 = \int_{k_c \cos \theta}^{\pi/\Delta x} \int_0^{2\pi} \omega^2 [\sin^2 \phi \sin^2 \theta + \cos^2 \theta]\, S(k, \phi) k\, dk\, d\phi \quad (27)$$

where $S(k, \phi)$ is the spectrum of the subresolution-scale waves, θ is the incidence angle, and k_c is the electromagnetic cutoff wavenumber in the two-scale model [14]. The summation in (25) incorporates both spatial and temporal variations in the radial velocity due to long waves. In the limit as $k \to 0$ and $\omega_{mn} T \to 0$, the contribution of a given wave component to the velocity variance is equivalent to that calculated for a surface with a constant acceleration. However, these contributions are added incoherently, so the spatial variations in σ_v^2 calculated from (25) are not necessarily the same as those obtained from a calculation of the acceleration effect.

The radar cross section is calculated in terms of a linear modulation transfer function, as discussed by Alpers *et al.* [15]. Thus, the radar cross section (averaged over Δx, Δy, and T) is given by

$$\sigma_0(x, y, t) = \bar{\sigma}_0[1 + f(x, y, t)] \quad (28)$$

where $\bar{\sigma}_0$ is the mean radar cross section for the entire scene, and

$$f(x, y, t) = \sum_{m=1}^{M-1} \sum_{n=1}^{N-1} a_{mn} b_{mn} R_{mn} \cdot \cos [k_m x + k_n y - \omega_{mn}t + \Phi_{mn} + \Phi_R] \quad (29)$$

where R_{mn} and Φ_R are the modulus and phase, respectively, of the radar modulation transfer function. This transfer function includes the effects of changes in the local slope of the surface (tilt modulation) as well as changes in the small-scale surface roughness (hydrodynamic modulation). Note that this modulation transfer function is equivalent to that discussed by Alpers *et al.* [15] and is k times the dimensionless MTF defined by Plant *et al.* [16]. For the case of tilt modulation, this transfer function may be written as

$$R_{mn} = k_n \sigma_0'(\theta)/\sigma_0(\theta) \quad (30)$$

and

$$\Phi_R = \pm \frac{\pi}{2} \quad (31)$$

where $\sigma_0(\theta)$ is the radar cross section of the surface as a function of incidence angle, and the sign of Φ_R is positive for look directions in the positive y-direction and negative for look directions in the negative y-direction [15]. Using a Bragg scattering model for $\sigma_0(\theta)$ and assuming a perfectly conducting surface and a Phillip's spectrum for the short waves, the tilt modulation transfer function may be written as

$$R_{mn} = \frac{4 \cot \theta}{1 \pm \sin^2 \theta} k_n \quad (32)$$

where the (+) plus sign holds for vertical polarization and the (−) minus sign is for horizontal polarization. Note that this transfer function goes to zero for azimuth-traveling waves ($k_n = 0$).

The hydrodynamic contribution to the modulation transfer function involves several possible mechanisms, including straining of short waves by long-wave orbital motions, modulation of the air flow across the long waves, and nonlinear effects such as wave breaking. Not all of these mechanisms are well understood on a theoretical basis, but intuitively one might expect the effects to depend on environmental conditions. Measurements of the modulation transfer function indicate a wind-speed dependence at X-band radar frequencies, but no apparent wind-speed dependence at L-band [16].

The simulation procedure described above yields the ensemble-averaged or expected value of the image intensity, which will be denoted by $I_0(x, y)$ in the following. The image intensity $I(x, y)$ observed with an actual SAR is influenced by coherent interference or speckle effects, which may be modeled as a multiplicative noise process, i.e.

$$I(x, y) = I_0(x, y)[1 + \epsilon(x, y)] \tag{33}$$

where $\epsilon(x, y)$ is a zero-mean random variable which has a variance of $1/N_l$, where N_l is the number of "looks" used in processing the data [17]. $\epsilon(x, y)$ also has spatial correlation statistics that are dependent on the SAR system bandwidth and are independent of scene motions [18].

If $I(x, y)$ is computed on a spatial grid with spacings larger than or equal to the nominal SAR resolution, the values of $\epsilon(x, y)$ may be considered to be uncorrelated from point to point. Thus, the spectrum of $\epsilon(x, y)$, which will be denoted by $S_\epsilon(k_x, k_y)$, is white. The spectrum of $I(x, y)$ can then be written as

$$S_I(k_x, k_y) = S_0(k_x, k_y) + S_n(k_x, k_y) \tag{34}$$

where $S_0(k_x, k_y)$ is the spectrum of $I_0(x, y)$, and $S_n(k_x, k_y)$ is the convolution of $S_0(k_x, k_y)$ with $S_\epsilon(k_x, k_y)$, which results in another white spectrum [19]. Thus, the expected value of the image spectrum is equal to the spectrum of $I_0(x, y)$ plus a constant noise floor. The mean value of this noise floor can be calculated using Parseval's theorem and the fact that

$$\langle I^2 \rangle = \langle I_0^2 \rangle (1 + 1/N_l) \tag{35}$$

which follows readily from (33), where the triangular brackets refer to average values over the entire image. From Parseval's theorem, the average over all wavenumbers of each term in (34) is proportional to the corresponding term in (35). Thus, the average or expected value of the noise floor is

$$\langle S_n \rangle = \langle S_0 \rangle / N_l \tag{36}$$

where $\langle S_0 \rangle$ is the average value of $S_0(k_x, k_y)$ over all wavenumbers, including $k_x = 0$, $k_y = 0$.

A measure of the wave contrast or detectability is given by the peak-to-background ratio, defined as the peak spectral density in the image spectrum divided by the noise spectral density. From the derivation presented above, this ratio may be expressed as

$$PBR = \frac{(S_I)_{\max}}{\langle S_n \rangle} = 1 + \frac{(S_0)_{\max}}{\langle S_0 \rangle} N_l \tag{37}$$

where $(S_0)_{\max}$ is the peak value in the spectrum of $I_0(x, y)$. A comparison of predicted values of this parameter with observed values is presented, along with comparisons of predicted and observed image spectra, in the following section.

III. Model Results

The simulation model described above has been exercised using wave height spectra measured by the NASA Radar Ocean Wave Spectrometer [20] during the SIR-B Southern Oceans experiment [7]. The results of these calculations are presented here and are compared with actual SIR-B image spectra. Additional results are also presented illustrating the imaging behavior for parameter variations not encountered during the SIR-B experiment.

Data were collected by the SIR-B sensor during orbit 91 on October 11, 1984 off the coast of Chile, and wave height spectra were measured nearly simultaneously in the same area by the ROWS system aboard a NASA P-3 aircraft. Detailed descriptions and intercomparisons of these data sets are given in Beal *et al.* [7]. Contour plots of the ROWS wave height and wave slope spectra are shown in Fig. 2(a) and (b). Note that the coordinate system is referred to the SIR-B ground track direction, which is horizontal on these plots.

The wave height spectrum shown in Fig. 2(a) was used in the SAR model described in the previous section, along with the other parameters listed in Table I. The radar modulation transfer function was evaluated from (32) at $\theta = 25°$, for horizontal polarization. This yields a dimensionless MTF having a magnitude of 10 and a phase of 90°. The contribution to the radial velocity variance from subresolution-scale waves was computed using a Pierson-Moskowitz spectrum [21] with a wind speed of 12 m/s. The velocity variance resulting from this calculation is approximately 0.21 $(m/s)^2$. The velocity variance contributed by waves longer than 50 m is a function of position, but has an average value of 0.19 $(m/s)^2$ for this case. The spectrum of the simulated SAR image intensity (I_0) is shown in Fig. 2(c), and the actual SIR-B image spectrum is shown in Fig. 2(d).

An intercomparison of the spectra shown in Fig. 2 shows that the slope spectrum, the simulated image spectrum, and the actual image spectrum are all similar in shape. The similarity between the simulated image spectrum and the slope spectrum results from the use of a dimensionless modulation transfer function that is independent of wavelength. Since both the dominant and secondary wave systems are nearly range-traveling, surface motion effects are minimal and the image is dominated by real modulation effects. The fact that the actual image spectrum has a similar shape supports the assumption of a wavelength-independent MTF. Although there are slight differences in the locations and relative magnitudes of the primary and secondary peaks, these differences are felt to be within the limits of experimental accuracy.

The ratio of the peak spectral density to the mean spectral density for the simulated image is

$$\frac{(S_0)_{\max}}{\langle S_0 \rangle} = 9.5 \tag{38}$$

for this case. From (37), this implies a peak-to-background ratio of 10.5 (for $N_l = 1$) when speckle effects are included. For the actual SIR-B image spectrum, a comparable value was obtained by computing the background

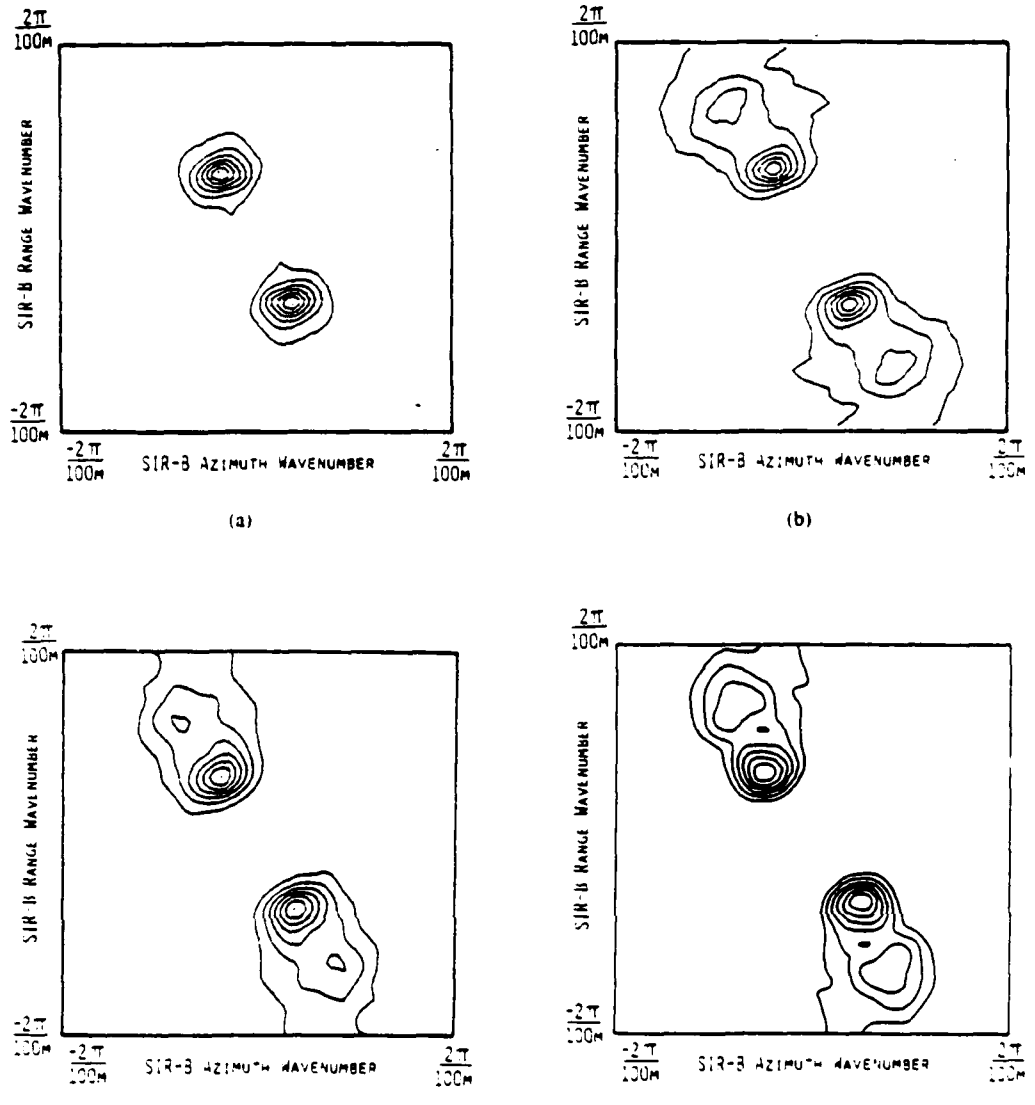

Fig. 2. Comparison of (a) wave height, (b) wave slope, (c) simulated image, and (d) actual SIR-B image spectra for orbit 91 (October 11, 1984).

TABLE I
ENVIRONMENTAL AND SAR SYSTEM PARAMETERS FOR ORBIT 91

Significant wave height	5.0 m
Local wind speed	12 m/s
SIR-B heading	34.2°T
Incidence Angle	35.1°
Platform Altitude	237 km
Platform Velocity	7500 m/s
Integration Time	0.66 sec
Pixel Spacing	25 × 25 m

spectral density along the right-hand side of the spectrum (at $k_r = 2\pi/100$ m). The ratio of the peak spectral density to this background value is 8.8.

The second SIR-B data set for which comparisons have been made was collected during orbit 106 on October 12, 1984. Contour plots for the ROWS wave height and slope spectra for this pass are shown in Fig. 3(a) and (b). The parameters used in the SAR model for this pass are given in Table II. The same value was assumed for the radar MTF as in the previous case. However, this parameter has almost no effect on the results of the simulation, since the dominant waves are traveling in the azimuth direction where the tilt MTF goes to zero. The radial velocity variance due to subresolution-scale waves was assumed to be the same as in previous case, and the variance contributed by longer waves is approximately 0.09 $(m/s)^2$ for this case. The simulated and actual SIR-B image spectra are shown in Fig. 3(c) and (d), respectively.

The simulated and actual image spectra are again quite similar in appearance to the slope spectrum for this data set. However, the similarity between the simulated image spectrum and the slope spectrum arises from a completely different mechanism in this case. The modulation of the backscattered power, as calculated from surface tilt ef-

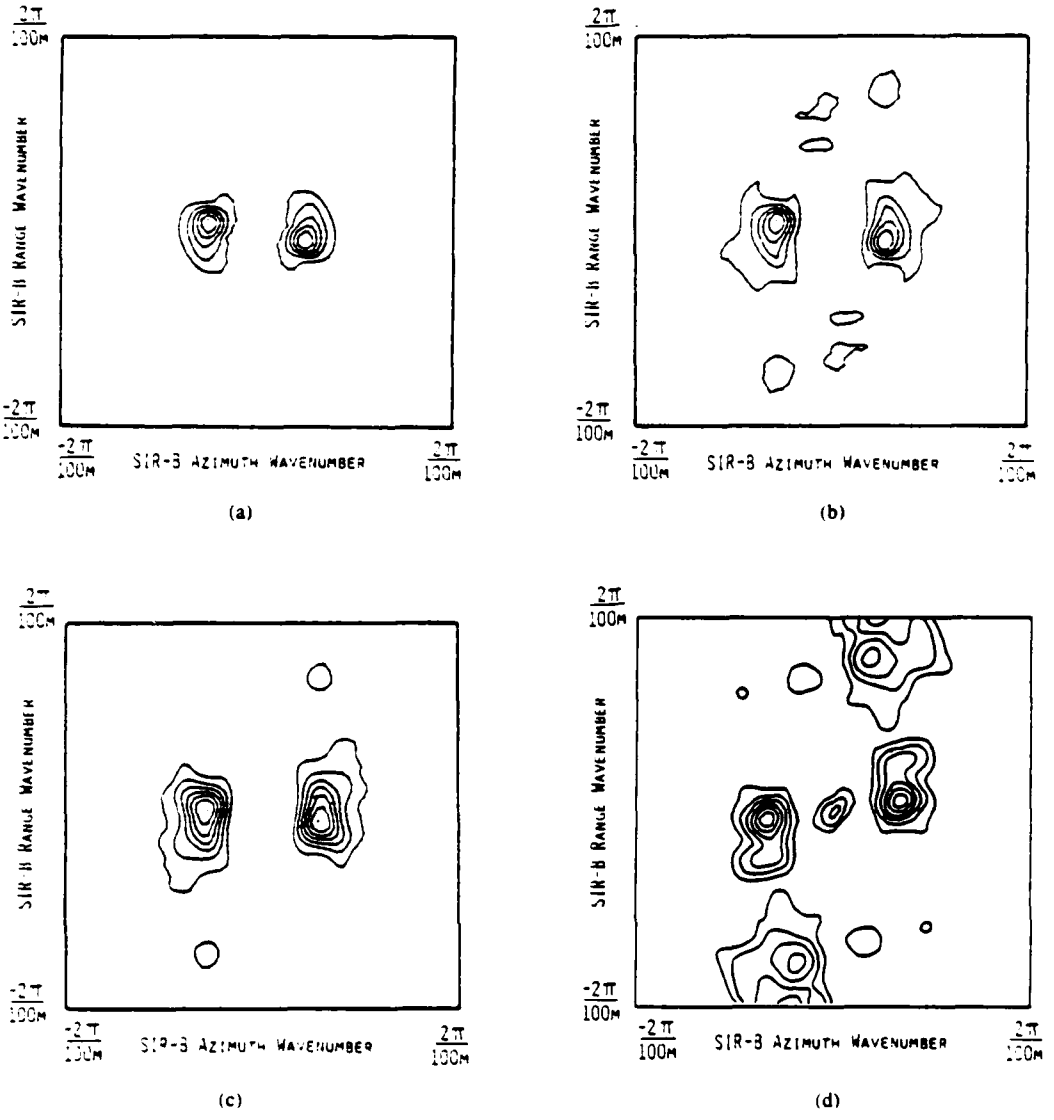

Fig. 3. Comparison of (a) wave height, (b) wave slope, (c) simulated image, and (d) actual SIR-B image spectra for orbit 106 (October 12, 1984).

TABLE II
ENVIRONMENTAL AND SAR SYSTEM PARAMETERS FOR ORBIT 106

Significant Wave Height	3.5 m
Local Wind Speed	12 m/s
SIR-B Heading	95.3°T
Incidence Angle	18.3°
Platform Altitude	237 km
Platform Velocity	7500 m/s
Integration Time	0.63 sec
Pixel Spacing	25 x 25 m

fects, is nearly zero for the dominant azimuth-traveling waves present in this pass. Thus, the calculated image intensity modulation is due almost entirely to surface motion (velocity bunching) effects. The apparent agreement between the calculated and observed spectra provides strong support for the assumed velocity bunching mechanism, although it does not rule out the possibility of other modulation mechanisms such as nonlinear hydrodynamic effects which might produce backscatter modulations for azimuth traveling waves.

The simulated image spectrum for this case has a normalized peak spectral density of

$$\frac{(S_0)_{max}}{\langle S_0 \rangle} = 3.1 \tag{39}$$

which yields a peak-to-background ratio of 4.1 from (37). The peak-to-background ratio of the actual image spectrum, calculated using the same procedure as described above, is 2.8. The difference between the observed and predicted values of the PBR may be due to additional noise sources affecting the background spectral density. The rather large difference between the PBRs for the two cases considered (8.8 for orbit 91 versus 2.8 for orbit 106) is predicted by the simulation model. This qualitative agreement, along with the similarity in shape between the sim-

ulated and actual image spectra, lends confidence to the simulation procedure. More extensive comparisons with observations over a wider range of conditions are needed to fully validate the model, however.

The effects of surface motions are dependent on the SAR system parameters (primarily the R/V ratio) as well as the surface conditions (as described by the wave height spectrum) and are most critical for waves traveling in the azimuth direction. In order to illustrate these effects over a wider range of conditions than occurred during the SIR-B experiment, the simulation model was operated for R/V values of 30, 60, and 120 s and for wave spectra having peak wavelengths of 100, 200, and 400 m in the azimuth direction. The pixel spacing was chosen to be 25 × 25 m in each case, and the integration times were assumed to be 0.56, 1.13, and 2.26 s for the three R/V values selected. These parameters are typical of spaceborne L-band SAR systems such as SIR-B (with R/V ranging from 30 to 60 s) and Seasat or ERS-1 (with $R/V \approx 120$ s). The incidence angle was taken as 25° in each case, and the radar modulation transfer function was assumed to be zero.

For the purpose of these illustrative calculations, a simple form was assumed for the wave height spectrum, as given by

$$S(k, \phi) = \frac{A \exp\left[-2(k_0/k \cos \phi)^2\right]}{\left[k^2 - 2kk_1 \cos \phi + k_0 k_1\right]^2} \quad -\frac{\pi}{2} < \phi < \frac{\pi}{2}. \tag{40}$$

This spectrum has a peak spectral density at $k = k_0$, $\phi = 0$, and has a frequency spectrum nearly identical to that proposed by Pierson and Moskowitz [21], if $A = 0.0013$, $k_0 = 0.59\ g/u^2$ and $k_1 = 0.4\ k_0$. This spectrum also has a frequency-dependent angular spreading which is similar to that inferred by Hasselmann *et al.* [22] from the JONSWAP 1973 data for frequencies above the spectral peak, and approaches the semi-isotropic Phillips spectrum for $k >> k_0$. Thus, this form appears to be a reasonable representation of the wave spectrum for a fully developed sea.

The wave spectrum defined by (40), with parameters selected to match the Pierson–Moskowitz spectrum, implies a significant wave height (H_s) of approximately 2 percent of the peak wavelength (which, incidentally, is roughly 30 percent larger than $2\pi g/\omega_p^2$, where ω_p is the peak frequency). In order to investigate the effects of changes in wave slope, runs were also made with the value of A reduced to yield a ratio $H_s/\lambda_p = 0.01$, where $\lambda_p = 2\pi/k_0$ is the peak wavelength. The wave spectrum used for the subresolution-scale waves was also reduced by one-half for these runs.

The results of these simulations are shown in Figs. 4 through 6. Fig. 4 shows the wave height and slope spectra and the corresponding image spectra for the case $\lambda_p = 200$ m and $R/V = 30$ s. Fig. 5 shows the ratio of the image spectrum to the wave height spectrum (hereafter referred to as the SAR transfer function) along the azimuth wavenumber axis for the same R/V ratio. The straight line in this plot indicates the velocity bunching transfer function

$$R_b^2 = \left(\frac{R}{V}\right)^2 gk^3 \cos^2\phi\ G^2(\theta, \phi) \tag{41}$$

defined by Alpers *et al.* [15], where

$$G^2(\theta, \phi) = \sin^2 \theta \sin^2 \phi + \cos^2 \theta \tag{42}$$

and $\phi = 0$ for the case under consideration. The SAR transfer function obtained from the simulations approaches this line (which indicates the mapping is in the "linear" regime) when the significant wave height is sufficiently small. For these cases (with $R/V = 30$ sec and $\lambda_p \leq 400$ m), the modulation produced by velocity bunching is larger than that which would be produced by tilt modulation if the waves were range-traveling. In the cases where the slope of the transfer function is near 2, the SAR image spectrum resembles the wave slope spectrum, as shown in Fig. 4(d).

When the wave height or R/V ratio increases, the transfer function begins to deviate from the value indicated by (41). For these cases, the transfer function can be approximately modeled as the product of (41) with an "azimuth falloff" function that is presumed to be related to the surface velocity distribution [6], [23]. Over certain wavenumber regions, the product of these two functions may be roughly constant, as in the (100, 1) and (200, 4) cases shown in Fig. 5. For this subset of cases, the SAR image spectrum more closely resembles the wave height spectrum, as shown in Fig. 4(c). When the wave height or R/V ratio increases further, the transfer function is dominated by the azimuth falloff effect, and the image spectrum becomes highly distorted.

An example of the effects of changing R/V are shown in Fig. 6. This plot of the SAR transfer function for $\lambda_p = 400$ m and $H_s = 4$ m indicates a gradual transition from the linear regime (for $R/V = 30$ s) to a moderately nonlinear regime (for $R/V = 120$ s). The azimuth falloff function for these cases can be approximated by

$$f^2(k_x) = \exp\left(-\sigma_x^2 k_x^2\right) \tag{43}$$

where σ_x has the value 17 m for $R/V = 30$ s, 34 m for $R/V = 60$ s, and 64 m for $R/V = 120$ s. These values are consistent with a velocity variance of approximately 0.32 $(\text{m/s})^2$, assuming the effective azimuthal impulse response function has the form

$$f(x) = \exp\left(-\frac{1}{2}\frac{Vx}{R\sigma_v}\right) \tag{44}$$

where σ_v^2 is the velocity variance, as discussed in Section II. This value is more than twice as large as the velocity variance calculated from (25) for this case, but is approximately equal to the total velocity variance for the assumed wave height spectrum. Thus, it appears that surface motions associated with all wavelength scales influence the azimuth falloff effect. This is consistent with

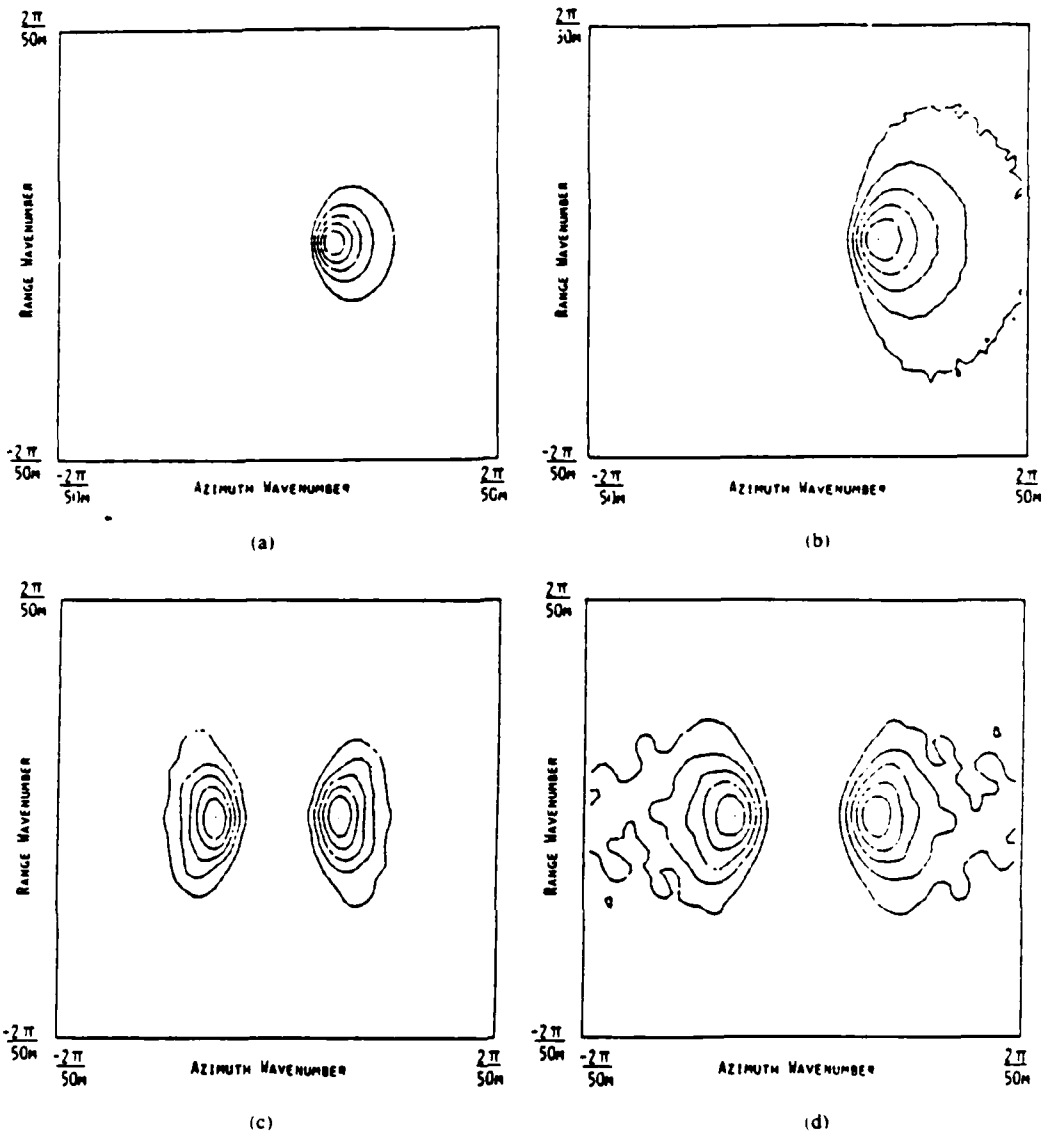

Fig. 4. Comparison of (a) wave height, (b) wave slope, and (c) simulated image spectra for R/V = 30 s, λ_p = 200 m, and H_s = 4 m, and (d) simulated image spectrum for R/V = 30 s, λ_p = 200 m, and H_s = 2 m.

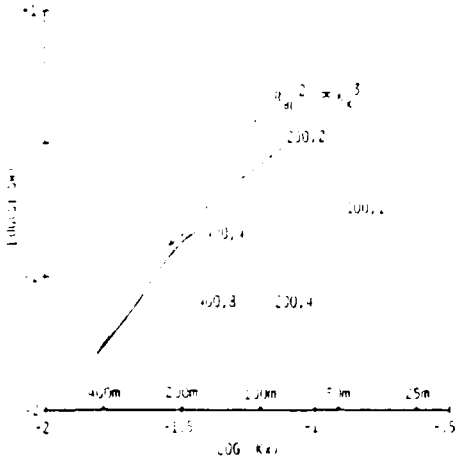

Fig. 5. Ratio of image spectrum to wave height spectrum along azimuth wavenumber axis for R/V = 30 s. Labels indicate dominant wave length (λ_p) and significant wave height (H_s). Solid line indicates the velocity bunching transfer function.

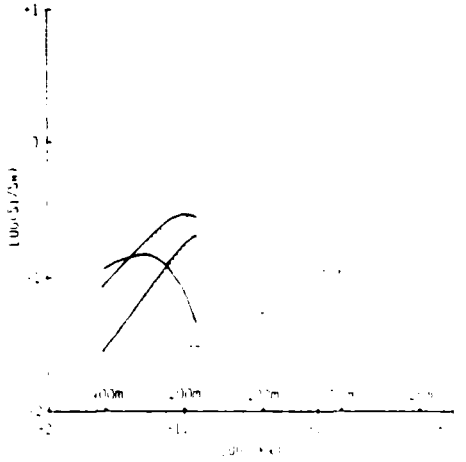

Fig. 6. Ratio of image spectrum to wave height spectrum along azimuth wavenumber axis for R/V = 30, 60, and 120 s, with λ_p = 400 m and H_s = 4 m. Solid curves indicate values obtained by simulations. Dotted curves indicate analytical fits discussed in text.

observations by Beal *et al.* [6] indicating that the azimuth falloff is dependent on the significant wave height.

An azimuth cutoff wavelength can be somewhat arbitrarily defined as

$$\lambda_c = \pi\sigma_r \tag{45}$$

which corresponds to the wavelength at which the falloff function reaches a value of approximately 0.018. λ_c is also roughly half the wavelength at which the total SAR transfer function reaches its peak value. The numerical values of λ_c for the examples shown in Fig. 6 are approximately equal to those predicted by Beal *et al.* [6] for a significant wave height of 4 m. Note that the peak value of the SAR transfer function decreases with increasing R/V for a given wave spectrum. Thus, for wavelengths near this peak, the wave contrast actually decreases with an increase in R/V, while the reverse is true for much longer wavelengths.

IV. Summary and Conclusions

The numerical model described in this paper indicates that for sufficiently small waveheight/wavelength and R/V ratios, the imaging of ocean waves by synthetic aperture radar may be considered to be a linear process, in the sense that the image spectral density at any given wavenumber (after correcting for image speckle effects) is proportional to the wave height spectral density at that wavenumber. Assuming that the constant of proportionality (or SAR transfer function) can be estimated, the wave height or slope spectrum can then be inferred from a measurement of the SAR image spectrum. For low-altitude spacecraft sensors such as SIR-B, this linear regime encompasses a reasonably large range of wave conditions. Predictions of image spectra for two SIR-B data sets agree reasonably well with actual image spectra and indicate that the imaging is within the linear regime for these cases.

As the wave height or R/V ratio increases, the imaging process enters a regime in which the ratio of the image spectrum to the wave height spectrum is dependent on some integrated property of the wave spectrum itself (possibly the significant wave height). In this case, estimating the wave height or slope spectrum from the SAR image is obviously more difficult, although it is conceivable that under certain circumstances, an iterative procedure might be used to accomplish this inversion. As the wave height or R/V ratio increases further, surface motion effects cause increasing distortions in the image spectrum and the possibility of estimating the wave height spectrum from the SAR image becomes more remote.

Acknowledgment

ROWS spectra were provided by F. Jackson of the NASA Goddard Space Flight Center. F. Monaldo of the Applied Physics Laboratory, Johns Hopkins University, supplied the SIR-B image spectrum contour plots and peak-to-background ratios used in this study. Helpful discussions with R. C. Beal and F. Monaldo are also acknowledged.

References

[1] F. I. Gonzalez, R. C. Beal, W. E. Brown, P. S. DeLeonibus, J. W. Sherman, J. F. R. Gower, D. Lichy, D. B. Ross, C. L. Rufenach, and R. A. Shuchman," Seasat synthetic aperture radar: Ocean wave detection capabilities," *Science*, vol. 204, pp. 1418-1421, 1979.

[2] W. McLeish, D. B. Ross, R. A. Shuchman, P. G. Teleki, S. V. Hsiao, O. H. Shemdin, and W. E. Brown, "Synthetic aperture radar imaging of ocean waves: Comparison with wave measurements," *J. Geophys. Res.*, vol. 85, pp. 5003-5011, 1980.

[3] S. S. Pawka, S. V. Hsiao, O. H. Shemdin, and D. L. Inman, "Comparisons between wave directional spectra from SAR and pressure sensor arrays," *J. Geophys. Res.*, vol. 85, pp. 4987-4995, 1980.

[4] D. J. Schwab, R. A. Shuchman, and P. C. Liu, "Wind wave directions determined from synthetic aperture radar imagery and from a tower in Lake Michigan," *J. Geophys. Res.*, vol. 86, pp. 2059-2064, 1981.

[5] R. A. Shuchman, W. Rosenthal, J. D. Lyden, D. R. Lyzenga, E. S. Kasischke, H. Gunther, and H. Linne, "Analysis of MARSEN X-band SAR ocean wave data," *J. Geophys. Res.*, vol. 88, pp. 9757-9769, 1983.

[6] R. C. Beal, D. G. Tilley, and F. M. Monaldo, "Large- and small-scale spatial evolution of digitally processed ocean wave spectra from Seasat synthetic aperture radar," *J. Geophys. Res.*, vol. 88, pp. 1761-1778, 1983.

[7] R. C. Beal, F. M. Monaldo, D. G. Tilley, D. E. Irvine, E. J. Walsh, F. C. Jackson, D. W. Hancock III, D. E. Hines, R. N. Swift, F. I. Gonzalez, D. R. Lyzenga, and L. F. Zambresky, "A comparison of SIR-B directional ocean wave spectra with aircraft scanning radar spectra," *Science*, vol. 232, pp. 1531-1535, 1986.

[8] W. R. Alpers and C. L. Rufenach, "The effect of orbital motions on synthetic aperture radar imagery of ocean waves," *IEEE Trans. Antennas Propagat.*, vol. AP-27, pp. 685-690, 1979.

[9] C. T. Swift and L. R. Wilson, "Synthetic aperture radar imaging of moving ocean waves," *IEEE Trans. Antennas Propag.*, vol. AP-27, pp. 725-729, 1979.

[10] R. O. Harger, "SAR ocean imaging mechanisms," in *Spaceborne Synthetic Aperture Radar for Oceanography*, R. C. Beal, P. S. DeLeonibus, and I. Katz, Eds. Baltimore, MD: Johns Hopkins Univ. Press, 1981, pp. 41-52.

[11] A. Jain, "SAR imaging of ocean waves: Theory," *IEEE J. Oceanic Eng.*, vol. OE-6, pp. 130-139, 1981.

[12] R. K. Raney, "Wave orbital velocity, fade, and SAR response to azimuth waves," *IEEE J. Oceanic Eng.*, vol. OE-6, pp. 140-146, 1981.

[13] W. Alpers, "Monte Carlo simulations for studying the relationship between ocean wave and synthetic aperture radar image spectra," *J. Geophys. Res.*, vol. 88, pp. 1745-1759, 1983.

[14] K. Hasselmann, R. K. Raney, W. J. Plant, W. Alpers, R. A. Shuchman, D. R. Lyzenga, C. L. Rufenach, and M. J. Tucker, "Theory of SAR ocean wave imaging: A MARSEN view," *J. Geophys. Res.*, vol. 90, pp. 4659-4686, 1985.

[15] W. R. Alpers, D. B. Ross, and C. L. Rufenach, "On the detectability of ocean surface waves by real and synthetic aperture radar," *J. Geophys. Res.*, vol. 86, pp. 6481-6498, 1981.

[16] W. J. Plant, W. C. Keller, and A. Cross, "Parametric dependence of ocean wave-radar modulation transfer functions," *J. Geophys. Res.*, vol. 88, pp. 9747-9756, 1983.

[17] L. J. Porcello, N. G. Massey, R. B. Innes, and J. M. Marks, "Speckle reduction in synthetic-aperture radars," *J. Opt. Soc. Amer.*, vol. 66, pp. 1305-1311, 1976.

[18] R. K. Raney, "SAR response to partially coherent phenomena," *IEEE Trans. Antennas Propagat.*, vol. AP-28, pp. 777-787, 1980.

[19] C. Wu, "Derivation of the statistical characteristics of SAR imagery data," in *Proc. 3rd ESA SAR Image Quality Workshop* (Frascati, Italy), pp. B2-B6, 1980.

[20] F. C. Jackson and W. T. Walton, "Aircraft and satellite measurement of ocean wave directional spectra using scanning-beam microwave radars," *J. Geophys. Res.*, vol. 90, pp. 987-1004, 1985.

[21] W. J. Pierson and L. Moskowitz, "A proposed spectral form for fully developed wind seas based on the similarity theory of S. A. Kitaigorodskii," *J. Geophys. Res.*, vol. 69, pp. 5181-5190, 1964.

[22] D. E. Hasselmann, M. Dunckel, and J. A. Ewing, "Directional wave spectra observed during JONSWAP 1973," *J. Phys. Oceanogr.*, vol. 10, pp. 1264-1280, 1980.

[23] M. J. Tucker, "The imaging of waves by satellite-borne synthetic aperture radar: The effects of sea-surface motion," *Int. J. Remote Sensing*, vol. 6, pp. 1059-1074, 1985.

David R. Lyzenga received the B.S.E. degree in physics from the University of Michigan in 1967, the M.S. degree in physics from Yale University in 1968, and the Ph.D. degree in electrical engineering from the University of Michigan in 1973.

He taught mathematics and physics at Calvin College in 1968–1969, and worked at the Space Physics Research Laboratory of the University of Michigan from 1970 to 1972. Since 1973, he has been employed by the Environmental Research Institute of Michigan (ERIM), where he has been involved in a variety of remote sensing projects involving both visible and microwave sensors. Since 1981, his primary research interest has been in the extraction of oceanographic information from synthetic aperture radar data. He is presently a Research Engineer in the Radar Science Laboratory at ERIM.

Dr. Lyzenga is a member of the American Geophysical Union, the Optical Society of America, Sigma Xi, Tau Beta Pi, and Phi Kappa Phi.

APPENDIX B

On the Estimation of Wave Slope- and Height-Variance Spectra from SAR Imagery

FRANK M. MONALDO AND DAVID R. LYZENGA

Abstract—A procedure is described for using synthetic aperture radar (SAR) imagery to estimate two-dimensional ocean wave slope- and height-variance spectra. The logic underpinning the procedure is based both on the results of the numerical simulation of SAR wave imagery and analytic descriptions of the SAR imaging process. The procedure, when applied to SAR imagery of waves acquired during the recent Shuttle Imaging Radar Mission (SIR-B), is shown to produce spectra that agree with independent measures of both the two-dimensional slope- and height-variance spectra. The implications of these results for future SAR missions aimed at measuring ocean waves are considered.

I. INTRODUCTION

HIGH-RESOLUTION SAR imagery has shown the potential of measuring ocean wave spectra. Using data from both spaceborne [1], [2] and a number of aircraft [3], [4] platforms, various investigators have demonstrated that spectral parameters such as wave number and propagation direction extracted from SAR image spectra are generally consistent with independent measures of the ocean surface. In high sea states though, a rotation of the wave vector toward the range (cross-track) direction can occur [1], [2], [5], [6].

In spite of voluminous imagery from both the Seasat SAR and various aircraft SAR systems, a generally acceptable procedure for generating estimates of the ocean wave slope- or height-variance spectrum from SAR imagery has not been found.

The basic problem is in specifying the relationship between SAR image intensity and either ocean surface wave height or slope. Although tower-based measurements of the relationship between local surface slope and radar cross section have yielded valuable information, the mapping of surface radar cross section into SAR image intensity is not direct. Because a SAR relies on Doppler information to achieve high azimuth (along-track) resolution, ocean surface movement causes the radar cross section associated with a particular spot on the ocean surface to be mapped into image intensity at a variety of locations in the final SAR image.

A second difficulty associated with prescribing a procedure for extracting wave spectra from SAR imagery is the lack of independently measured two-dimensional ocean wave spectra over scales comparable to SAR image spectra. Without such independent spectra, it is impossible to verify ocean slope- or height-variance spectra estimates from SAR imagery.

These two difficulties have been alleviated by two recent developments: 1) a sufficiently complete SAR imaging theory to allow complete two-dimensional modeling, both analytic [7] and numerical [8], [9], of the SAR wave imaging process, and 2) new methods of measuring the two-dimensional ocean wave spectrum with high spectral resolution.

Alpers *et al.* [7] have described a linear systems approach to the SAR imaging process that provides a basis for a procedure to estimate wave height spectra from SAR image spectra. Monaldo [6] has demonstrated the additional value of treating the indirect and formally nonlinear mapping of surface radar cross section into various pixel locations in the SAR image as a low-pass filter in a linear system so as to retain the advantages of tractability inherent in a linear systems approach.

The limits to the effectiveness of a linear systems approach to SAR wave imaging can be explored through the use of numerical simulations. SAR wave image simulations have been implemented by Alpers [8] and Lyzenga [9]. The simulations begin with an arbitrary input ocean spectrum, construct the corresponding ocean surface height topography, use models for the modulation of the backscatter as function of wave height, and include the indirect mapping of intensity caused by surface motion to form a SAR image. A spectrum of the image is computed and then compared to the input ocean spectrum. In this paper, the numerical SAR wave image modeling, as implemented by Lyzenga, is used to address the limits of treating the effect of ocean surface motion as a low-pass filter.

In the seven years since the launch and subsequent demise of Seasat, at least two airborne techniques for the measurement of directional ocean wave spectra have matured: the surface contour radar (SCR) [10] and the radar ocean wave spectrometer (ROWS) [11]. These instruments have been shown to reliably measure the two-dimensional ocean surface wave spectrum with wavenumber and angular resolution comparable to that obtained from a typical SAR image spectrum.

The Shuttle Imaging Radar Mission (SIR-B) aboard the shuttle Challenger permitted the execution of an experi-

Manuscript received November 5, 1985; revised February 3, 1986.

F. M. Monaldo is with the Applied Physics Laboratory, the Johns Hopkins University, Laurel, MD 20707

D. R. Lyzenga is with the Radar Division, Enviromental Research Institute of Michigan, Ann Arbor, MI 48107

IEEE Log Number 8608582.

ment where SAR imagery was obtained in regions spatially and temporally coincident with measurements of the ocean wave spectrum by the SCR and ROWS mounted aboard a NASA P-3 aircraft. Preliminary results from the experiment are reported in [12].

The P-3 also was equipped with two other wave measuring instruments: 1) the advanced airborne flight experiment (AAFE) altimeter, which used the spreading of a narrow nadir-transmitted radar pulse to estimate the total height variance of the surface, and an airborne optical lidar (AOL), which provides wave height profiles along the aircraft flight direction that can be subsequently processed to yield one-dimensional ocean wave spectra.

In October, the highest sea states are generally found at far southern latitudes. For this reason, the experiment was staged out of Punta Arenas, Chile, near the southern tip of South America. During the actual experiment, SAR imagery with coincident aircraft measurements were acquired over a five-day period. By applying the algorithm described in this paper, we were able to generate estimates of two-dimensional ocean height-variance spectra that closely agree with measurements made by both the ROWS and SCR [12].

The general strategy used in this work has been to develop algorithms to convert SAR imagery into height-variance spectra based on both analytic models and experience in dealing with speckle noise inherent in SAR imagery. The effectiveness of the algorithms are then verified by the numerical simulations and comparisons with independently measured wave spectra.

II. SAR Wave Imaging Mechanisms

At typical incidence angles (20° to 60°), a SAR interacts with the ocean surface through a "Bragg" resonance mechanism with short ocean surface waves [13]. The radar cross section of the surface is dependent on the local incidence angle and the height-variance spectral density of the surface at the Bragg wavenumber. In the case of *L*-band SAR, like Seasat and SIR-B, the Bragg waves are in the decimeter wavelength regime. The modulation of radar cross section by long (>50 m) waves renders the long waves visible in real aperture radar as well as SAR imagery. In addition, SAR imagery is influenced by the motion of the surface, with the result that long waves may be either more or less visible in a SAR image than in a real aperture radar image with the same nominal resolution.

The modulation of the backscattered power that is caused by changes in the local incidence angle is designated as the tilt effect. The modulation in power caused by changes in the spectral density at the Bragg wavenumber across the profile of the long waves is called the hydrodynamic effect. Changes in Bragg wave spectral density are due to interactions of these short surface waves with the local currents induced by the longer waves, and also may include other effects such as those due to variations of wind speed over the long wave profile. These effects are environmentally dependent and generally not well understood [14]–[16].

The term "radar modulation transfer function" is used to define the relationship between ocean surface wave height and the radar return [7]. The effect of local slope variations is described by the tilt modulation transfer function

$$R_t = ik_r \frac{1}{\sigma_0}\left(\frac{\partial \sigma_0}{\partial \theta}\right) \tag{1}$$

where k_r is the range component of ocean wavenumber, σ_0 is the radar cross section of the surface, and θ is the incidence angle [7]. Note that the phase of this transfer function is $\pm 90°$ with respect to the long wave crest, depending on the propagation direction of the wave (i.e., the sign of k_r). The magnitude of R_t can be estimated by using the expression for $\sigma_0(\theta)$ obtained from the Bragg scattering model [13], i.e.,

$$\sigma_0(\theta) = 16\pi k_0^4 g^2(\theta)\, S(2k_0 \sin\theta) \tag{2}$$

where k_0 is the radar wavenumber, $S(k)$ is the wave height-variance spectral density, which is evaluated at the Bragg wavenumber, and $g(\theta) = 1 \pm \sin^2\theta$ for a perfectly conducting surface where the upper sign (+) holds for vertical polarization and the lower (−) sign for horizontal polarization. Assuming a Phillips spectrum for the short waves, i.e., $S(k) = Ak^{-4}$, where k is surface wavenumber magnitude, the tilt modulation transfer function may be approximated by

$$R_t = ik_r \frac{4\cot\theta}{1 \pm \sin^2\theta} \tag{3}$$

over the range of incidence angles for which Bragg scattering is valid.

A similar transfer function can be defined for hydrodynamic modulation. Theoretical calculations of this transfer function, based on interactions of the Bragg waves with the orbital currents associated with longer waves, indicate a magnitude of $4.5k_r^2/k$ [7], assuming a Phillips spectrum for the short waves and the relaxation constant is zero. This is roughly a factor of two smaller than the magnitude of the tilt modulation transfer function at $\theta = 25°$.

The effects of surface motions on the SAR imaging process may be divided into two categories. First, the orbital velocities associated with a given wave component cause periodic displacements within the SAR image that result in a periodic modulation of the image intensity. If these displacements are small compared to the azimuthal component of wavelength, the image modulations caused by this "velocity bunching" effect may be described by a transfer function whose magnitude is given by

$$R_v = \frac{R}{V}\omega k_a(\sin^2\theta \sin^2\phi + \cos^2\theta)^{1/2} \tag{4}$$

where R is the range between the SAR platform and the surface, V is the platform ground track velocity, ω =

$\sqrt{gk}$ is the radian frequency of the ocean wave, k_a is the azimuth wavenumber, and $\sin \phi = k_r/k$ [7]. If the incidence angle θ is small, this transfer function reduces to

$$R_v = \frac{R}{V} \sqrt{gk}\, k_a \cos \theta. \tag{5}$$

The phase of the velocity bunching modulation transfer function, to this level of approximation, is either zero or 180°, depending on the sign of k_a.

At near nadir incidence ($\lesssim 30°$), the magnitude of the tilt modulation transfer function dominates the hydrodynamic modulation transfer function. Therefore, we have chosen to approximate SAR wave imaging at near nadir incidence by the addition of the tilt and velocity bunching modulation terms. The ultimate justification of the utility of this approximation rests in its effectiveness in estimating slope- and height-variance spectra from SAR imagery.

The effects of velocity bunching and tilt modulation may be combined by adding these complex modulation transfer functions. Since these transfer functions are orthogonal (i.e., their phases differ by $\pm 90°$), the squared magnitude of the combined transfer function is the sum of the square magnitude of each, i.e.,

$$R_{SAR}^2 = \mu^2 k_a^2 + m^2 k_r^2 \tag{6}$$

where

$$\mu = \frac{R}{V} \sqrt{gk} \cos \theta \tag{7}$$

and

$$m = \frac{4 \cot \theta}{1 \pm \sin^2 \theta}. \tag{8}$$

When the wave amplitude becomes sufficiently large, so that the maximum scatterer displacements caused by the orbital motion are larger than roughly one-quarter of the azimuth wavelength, the velocity bunching process becomes nonlinear in the sense that a further increase in wave amplitude or wave height-variance spectral density does not result in a proportional increase in image intensity-variance spectral density at the same wavenumber.

This effect, along with the effects of the variations in the surface velocity within each resolution cell and during the SAR integration time, form a second category of motion effects. These effects cause a departure from the behavior predicted by (6). Numerical simulations [9] indicate that these effects may be accounted for by multiplying the transfer function given in (6) by an azimuthal weighting or falloff function. In effect, the image displacements, due to ocean surface motions that are uncorrelated with the dominant wave system, smear the image in azimuth. The azimuth falloff function, therefore, can be thought of as a low-pass filter. In Section V, this will be discussed in more detail.

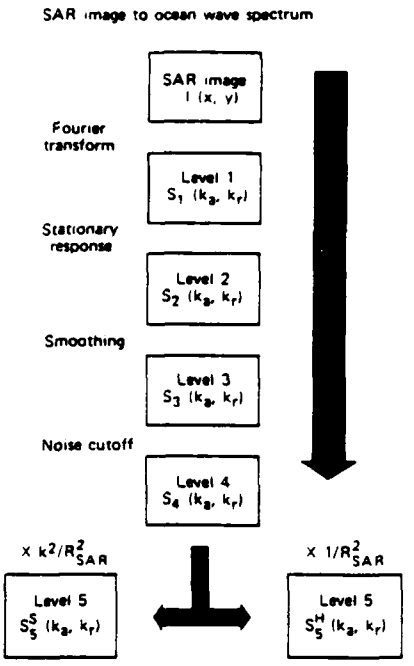

Fig. 1. Outline of procedure to estimate ocean wave slope- and height-variance spectra from SAR imagery.

III. The Estimation of Wave Height Spectra from SAR Imagery

The procedure used to estimate two-dimensional slope- and height-variance spectra from SAR imagery can be broken into a five-level process outlined in Fig. 1. It is important to begin with SAR images that are both radiometrically corrected and geometrically rectified. For the SIR-B mission, such imagery has been provided to us by the Jet Propulsion Laboratory.

From SAR intensity imagery, a single SAR image frame can be extracted. Such a frame is comprised of 512 × 512 image pixels. Since each pixel represents a 12.5 m × 12.5 m area, the entire image frame corresponds to a 6.4 km × 6.4 km patch on the ocean surface. This frame size provides a sufficiently large area that at least 10 cycles of very long surface waves, up to 640 m in length, can be included in a single image frame. They are also small enough that the ocean can be reasonably assumed homogeneous within a frame [12].

The mean image intensity is subtracted from the image frame and divided into the result. This image of fractional modulation is then Fourier transformed and squared to produce a level 1 image intensity-variance spectrum as a function of azimuth and range wavenumber $S_1(k_a, k_r)$.

Because a SAR image has finite resolution in both the azimuth and range directions, spectral response in a level 1 spectrum falls off at high azimuth and range wavenumbers. The estimation of and correction for this falloff in response has been reported elsewhere [2], [17]. We have designated this correction as the stationary response correction to distinguish this spectral response function from the falloff in spectral response caused by ocean surface motion, which will be discussed later. The stationary re-

sponse function is estimated by examining SAR imagery of homogeneous, spectrally white scenes. The falloff is fit to a model function which is then inverted and used as a multiplicative correction to the image spectrum. After this correction, the result is a level 2 spectrum $S_2(k_a, k_r)$.

Because this level 2 spectrum has only 2 degrees of freedom, the value of the spectrum at each two-dimensional wavenumber bin is a very noisy representation of the underlying spectrum. The underlying spectrum is the one that in principle would be the limit obtained by the ensemble average of many spectral measurements. Specifically, for only 2 degrees of freedom, the rms fractional error in each spectral estimate is 100 percent.

To alleviate this problem, the level 2 spectrum is convolved with a Gaussian-shaped kernel sufficiently wide that each spectral estimate in the level 3 spectrum has about 300 degrees of freedom with an associated rms error of only 8.5 percent [2]. Of course, in the level 3 spectrum adjacent spectral estimates are no longer statistically independent causing a reduction in resolution in wavenumber space.

It is possible at this point to further reduce the uncertainty by averaging level 3 spectra from adjacent image frames. Assuming the ocean surface is spatially homogeneous over these frames, the averaged spectra still will have greater statistical reliability. The decision to average adjacent spectra is dependent on the particular oceanographic situation considered. In regions of the ocean far from current boundaries and high winds, it might be reasonable to average spectra over large areas. In regions where spectra might be more rapidly spatially evolving, further averaging spectra would not be justified.

SAR imagery is contaminated by the presence of speckle noise. As the number of incoherent looks averaged to form a SAR image increases, the level of noise is reduced. This muliplicative noise also will contaminate spectra of the SAR imagery. The amount of noise present in the spectrum is dependent on both the mean image intensity and the image intensity variance caused by waves in the image [18].

In addition to the speckle noise present in both the SAR imagery and resultant spectra, there appears to be another source of broad-band spectral noise. One possible source is a "spikiness" in the radar return, which would produce a strongly peaked spatial autocorrelation function of the radar cross section, or equivalently a broad spatial spectrum of the radar cross section. Unlike the effects of speckle, the contribution of such radar signal spikes to the SAR image spectrum would be modified by the motion-induced azimuth falloff function. Clearly, more research is needed to understand the source of these effects. However, in most cases, an empirical procedure can be followed to separate the noise floor from the "true" spectrum.

To remove the effects of broad-band noise in the spectra, we generate level 4 spectra by subtracting a constant from all spectral values in the level 3 spectrum. Any negative values are set equal to zero. The constant level to be subtracted is calculated using the results from Goldfinger [18].

As mentioned in the previous section, the SAR modulation transfer function defines the relationship between the SAR image spectrum and the ocean height-variance spectrum. Employing (6) we relate a level 4 spectrum to a level 5 height-variance spectrum by

$$S_5^H(k_a, k_r) = \frac{S_4(k_a, k_r)}{R_{SAR}^2} = \frac{S_4(k_a, k_r)}{m^2 k_r^2 + \mu^2 k_a^2} \tag{9}$$

$S_5^H(k_a, k_r)$ is the level 5 estimate of the height-variance spectrum of the ocean surface. Similar, the slope-variance spectrum $S_5^S(k_a, k_r) = k^2 S_5^H(k_a, k_r)$ can be estimated

$$S_5^S(k_a, k_r) = \frac{S_4(k_a, k_r)\, k^2}{R_{SAR}^2} = \frac{S_4(k_a, k_r)\, k^2}{m^2 k_r^2 + \mu^2 k_a^2}. \tag{10}$$

Although the integral over wavenumber space of level 5 spectra given in (9) and (10) ought to yield estimates of the total height or slope variance of the ocean surface, the normalization of the image spectrum is not yet well understood. As a more reliable procedure, level 5 spectra can be normalized to height variance or slope variance measured independently. Eventually, we anticipate that further analysis of SIR-B and independently measured wave spectra will result in more accurate estimates of the total modulation transfer function.

IV. Comparison between SAR and Independently Measured Wave Spectra

The instruments aboard the NASA P-3 aircraft, which measured wave spectra in the vicinity of SAR imagery, allow us to verify the above procedure for estimating wave spectra from SAR imagery. Fig. 2 shows a set of four spectra. The spectrum on the upper left is a level 5 SAR slope spectrum from SIR-B imagery off the coast of Chile on Shuttle orbit 91. Note that azimuth wavenumber direction is parallel to and the range wavenumber direction is perpendicular to the spacecraft flight direction. The spectrum on the upper right is a Radar Ocean Wave Spectrometer (ROWS) [11] estimated slope-variance spectrum measured from the P-3 aircraft approximately 3 h after the shuttle overpass at the same spot in the ocean. Note the extreme similarity in the spectra. Both show a bimodal wave system with peaks in each spectrum showing similar relative magnitude.

The peaks in the SAR spectra from orbit 91, however, are predominantly range traveling. Azimuth traveling waves are somewhat more problematic for measurement by a SAR. The spectrum in the lower left of Fig. 2 is a level 5 slope spectrum from SIR-B orbit 106 off the coast of Chile. The peak energy system is almost exactly azimuth traveling with a wavelength of approximately 350 m. A secondary wave system also is propagating in the range direction. The lower right-hand corner of Fig. 2 shows the corresponding slope-variance spectrum from the ROWS. Although the spectra are separated by about 50

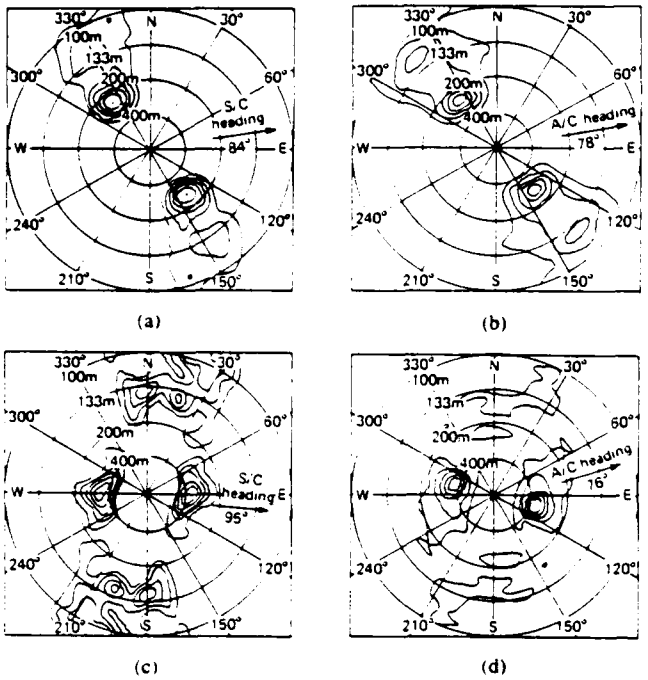

Fig. 2. Comparison of ROWS and SAR estimates of slope-variance spectra. (a) Level 5 SAR slope spectrum for orbit 91, time: 0230 October 11, 1984 (GMT), location: 55.5°S, 82.5°W. (b) ROWS slope spectrum, time: 0330 October 11, 1984 (GMT), location: 55.3°S, 81.2°W. (c) Level 5 SAR slope spectrum for orbit 106, time: 0045 October 12, 1984 (GMT), location: 56.00°S, 82.0°W. (d) ROWS slope spectrum, time: 0400 October 12, 1984 (GMT), location: 55.5°S, 81.5°W. Extracted from [12].

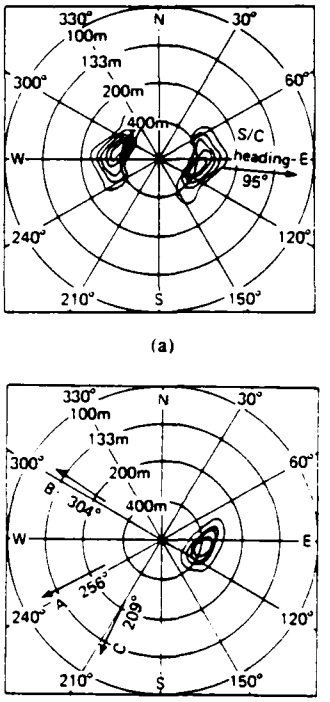

Fig. 3. Comparison of SCR and SAR estimates of height-variance spectra. (a) Level 5 SAR height spectrum for orbit 106, time: 045 October 12, 1984 (GMT), location: 56.0°S, 82.0°W. (b) SCR height spectrum obtained from composite of three flight headings (209°, 256°, and 304° with respect to North) on October 12, 1984. Extracted from [12].

km, they both confirm the existence of both wave systems.

The comparison of level 5 SAR slope spectra with actual measurements of slope-variance spectra from the P-3 aircraft strongly support the conclusion that level 5 SAR slope spectra are reasonable estimates of the ocean slope-variance spectrum.

Fig. 3 shows a comparison of the level 5 height spectra from SIR-B with corresponding height-variance spectra measured by the Surface Contour Radar (SCR) [10] for orbit 106. The SCR was not operating during orbit 91. Again note the similarity between the spectra. Of course, the k^2 conversion between the slope and height spectra tends to suppress high-frequency peaks apparent in the slope spectra. For this data set, the level 5 SAR height spectra are highly correlated to independently measured wave height spectra.

In our discussion thus far, we have not considered any correction for the falloff in azimuth response associated with ocean surface motion [6], [19]. A reliable systematic procedure to perform this correction is still under development. As was discussed in Section II and will be pointed out in Section V, the effect of ocean surface motion on a SAR image is proportional to the R/V ratio of the SAR platform. Because SIR-B orbited at a 230-km altitude as opposed to the 800-km altitude of Seasat, the R/V ratio for SIR-B is approximately 35 s as compared to the Seasat R/V ratio of 120 s. The next section will demonstrate that for all but the most extreme sea states, the azimuth falloff only minimally affects SIR-B spectra out to a wavenumber of $2\pi/(100\text{ m})$ or 0.0628 rad/m, which are the outer limits of the spectra displayed in Figs. 2 and 3. Therefore, we leave this correction for the future.

V. The Limitations of SAR Imagery in High Sea States

A SAR relies on Doppler information to achieve its high azimuth resolution. Ocean surface motion, which alters this Doppler information, serves to complicate the imaging process. In Section II, the advection of surface scatterers by the orbital velocity of ocean surface waves is shown to be the source of the velocity bunching wave imaging mechanism for azimuth traveling waves.

Velocity bunching serves to make azimuth traveling waves visible in SAR imagery because surface velocities are modulated on the spatial scale of the long ocean wave and are highly correlated with the ocean surface slope of that wave. However, the orbital velocities imparted to surface scatterers are not all spatially correlated. The motion of scatterers induced by waves of wavelengths smaller than or of the same order of the SAR spatial resolution certainly do not contribute to the imaging of waves. Even at large spatial scales, some fraction of the velocity variance on the ocean surface is sufficiently random that it is destructive to the image forming process. Depending on the particular SAR configuration and the sea state, SAR spectral response falls rapidly with azimuth wavenumber.

At sufficiently large azimuth wavenumbers, no constructive imaging is possible.

In this section we will endeavor to provide a heuristic explanation for this lack of azimuth response. The results of numerical simulations and measurements made from actual SAR spectra are presented and interpreted in the context of this heuristic explanation.

Essentially we will model the effect of ocean surface motion as a linear low-pass filter applied to SAR imagery. For a scatterer with a velocity v_r parallel to the SAR radar beam, the scatterer will be displaced in azimuth in the SAR image by an amount Δx given by

$$\Delta x = \frac{R}{V} v_r. \tag{11}$$

If we assume that the spatially random portion of surface velocity variance radial to the SAR is described by a Gaussian probability distribution with rms velocity v_σ, then the azimuth position shifts of the surface scatterers also will be Gaussian distributed with an rms position shift given by

$$x_\sigma = \frac{R}{V} v_\sigma. \tag{12}$$

These random position shifts can be thought of as smearing the SAR image in the azimuth direction or equivalently of convolving the unsmeared SAR image with an impulse response function $h(x)$ given by

$$h(x) = \frac{1}{\sqrt{2\pi} x_\sigma} \exp\left[-\frac{x^2}{2x_\sigma^2}\right]. \tag{13}$$

This convolution in the SAR image spectrum is equivalent to multiplying the SAR image spectrum of the unsmeared image by

$$H(k_x) = \exp\left[-\frac{k_x^2}{2k_\sigma^2}\right] \tag{14}$$

where k_σ is given by

$$k_\sigma = \frac{V}{\sqrt{2} R v_\sigma}. \tag{15}$$

This k_σ is the azimuth wavenumber where spectral response falls to 0.61 of its maximum value. We define λ_σ as the wavelength associated with k_σ where λ_σ is given by

$$\lambda_\sigma = 2\pi \sqrt{2} \frac{R}{V} v_r. \tag{16}$$

The quantity λ_σ is not literally the azimuth "cutoff" wavelength, since azimuth traveling waves somewhat shorter than λ_σ can be imaged. Experimental observations and numerical simulations of SAR imagery discussed below indicate that, for the spectral smoothing described in Section III, the azimuth cutoff wavelength is about one-half λ_σ.

Attempts to estimate v_σ have been made by Beal *et al.* [1] and Thomas [20], [21]. Clearly, v_σ is, in general, dependent upon both the ocean height-variance spectrum and relative SAR geometry. Since Seasat had a nadir incidence angle of 20° and wave imagery obtained from SIR-B is generally at similar nadir angles, we can reasonably neglect geometric considerations and consider only the vertical component of orbital velocity as being parallel to the radar beam. At 20° from nadir, results should be accurate to about 10 percent.

If $S(\omega)$ is defined as the one-dimensional height-variance frequency spectrum, then $\omega^2 S(\omega)$ is the velocity-variance frequency spectrum. For deep water waves, the vertical component of orbital velocity is equivalent to the horizontal component and is given by

$$v_\sigma = \left[\int_{\omega_1}^{\omega_2} \omega^2 S(\omega)\, d\omega\right]^{1/2}. \tag{17}$$

The velocities contributing to (17) may be considered as the velocities of scattering patches or facets in a two-scale model [22]. Thus, the upper limits of integration ω_2 should correspond to the cutoff wavenumber in the two-scale model. However, the contributions from waves shorter than this cutoff is usually very small. Therefore, for the purpose of these calculations, the upper limits of integration ω_2 can be taken to be infinity.

Tucker [20] has suggested that only surface velocities induced by waves with wavelengths less than twice the SAR resolution limit contribute to the smearing. Selecting the lower limit of integration to correspond to the frequency of a wave having a wavelength λ_1 equal to twice the resolution of the SAR, and assuming that $S(\omega)$ has the general form of the Pierson-Moskowitz spectrum [23], the appropriate rms velocity that contributes to smearing is given by

$$v_\sigma = (0.442 \text{ m}^{1/2}/\text{s})\, H_s^{1/2} [\text{erf}\,(2.86 \times 10^{-2} \lambda_1 H_s)]^{1/2} \tag{18}$$

where H_s is significant wave height. The corresponding λ_σ is

$$\lambda_\sigma^A = (3.93 \text{ m}^{1/2}/\text{s}) \frac{R}{V} H_s^{1/2} [\text{erf}\,(2.86 \times 10^{-2} \lambda_1 H_s)]^{1/2} \tag{19}$$

If we assume that velocities at all spatial scales contribute to azimuth smearing, i.e., $\lambda_1 \to \infty$ the worst case assumption, (19) reduces to

$$\lambda_\sigma^B = (3.93 \text{ m}^{1/2}/\text{s}) \frac{R}{V} H_s^{1/2}. \tag{20}$$

Regardless of what fraction of the total surface velocity variance contributes to azimuth smearing, (19) and (20) make clear the critical dependence of azimuth smearing on the R/V ratio of the SAR platform.

These results may be compared with numerical simulations of SAR image spectra. Fig. 4 shows the total

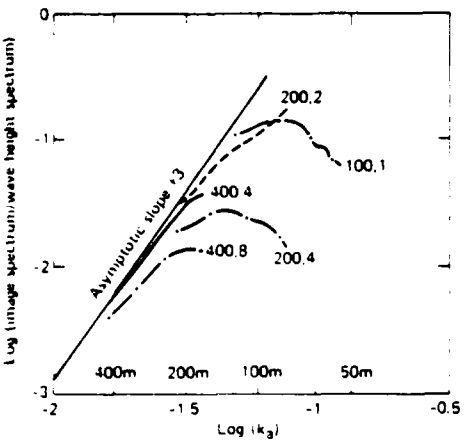

Fig. 4. Ratio of image spectrum to height spectrum along azimuth wavenumber axis for R/V = 30 s obtained from numerical simulation of SAR image spectra. First number associated with each curve indicates dominant wavelength (in meters), the second indicates significant wave height (in meters). Extracted from [9].

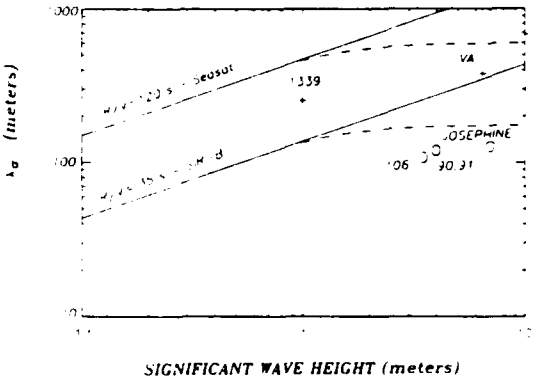

Fig. 5. A comparison of λ_a estimated from (19) and (20) and the Seasat and SIR-B R/V ratios. Solid lines refer to (20), dashed lines to (19) assuming λ_1 = 50 m. Crosses marked λ_a's estimated from actual Seasat SAR image spectra. Circles marked λ_a's estimated from SIR-B SAR image spectra. The numbers refer to orbit numbers, the names refer to hurricanes in the vicinity of SAR imagery.

TABLE I
COMPARISON OF PREDICTED λ_a USING A NUMERICAL SIMULATION AND (19) AND (20) FOR VARIOUS SIGNIFICANT WAVE HEIGHTS AND DOMINANT WAVELENGTHS
(R/V = 30 s.)

Significant wave height (meters)	Dominant wavelength (meters)	λ_a Simulations (meters)	λ_a^A Equation (19) (meters)	λ_a^B Equation (20) (meters)
2	100	192	139	167
4	200	235	147	235
8	400	305	150	334
	100	147	68	82
2	200	127	71	116
4	400	158	74	167

transfer function obtained from the simulation model described in [9] for five different wave conditions. The cases for which the significant wave height is equal to two percent of the dominant wavelength correspond to fully developed Pierson–Moskowitz spectra. The remaining cases use the same spectral shape, but have a total significant wave height reduced by a factor of two.

The transfer functions in Fig. 4, shown for the azimuth wavenumber direction, may be fit quite closely by the product of (19) and (14) with the values of k_σ shown in Table I. The corresponding λ_σ's also are shown in Table I along with λ_σ^A and λ_σ^B computed from (19) and (20), respectively.

The results for the fully developed spectra shown in the Table indicate that the azimuth falloff functions obtained from the numerical simulations are closer to the predictions of (20), i.e., the integration of velocity variance over the entire spectrum, than the predictions using (19). That is, the calculations agree reasonably well with the numerical simulations based on the Pierson–Moskowitz spectrum.

The agreement is also good for the cases where the significant wave height of the Pierson–Moskowitz spectrum is reduced by a factor of two, except for the shortest wavelength (100 m) case considered. In this case, the departure from a "linear" transfer function appears to be caused by nonlinearities in the imaging of the dominant wave itself, whereas in the other cases, the smearing effects from random surface motion are most important. That is, for this particular case, the treatment of the effects of ocean surface motion as a low-pass filter in a linear system starts to break down. Except for this case, the SAR imaging simulation supports the conclusion that the effects of motion generally can be treated as a low-pass filter on a linear system.

To examine how well the analytic and numerical modeling describe the azimuth falloff problem, we estimated the falloff observed in a series of SAR spectra from both Seasat and SIR-B. The estimate of the azimuth falloff was performed by excluding from consideration the regions in each spectrum having apparent concentrations of wave spectral energy. The remaining regions of the spectrum exhibited a gradual spectral energy falloff in the azimuth direction resting on a relatively low flat platform of spectral energy density.

After subtraction of this platform, the spectral falloff was fit, in a least squares sense, to the Gaussian-shaped azimuth falloff as suggested by (14). The resulting fit yielded the parameter k_σ or alternatively λ_σ.

Fig. 5 compares estimates of azimuth falloff for various SAR image spectra from Seasat and SIR-B with expected values of λ_σ. The solid lines represent the limiting case, where all velocities contribute to azimuth smearing, yielding λ_σ^B proportional to $H_s^{1/2}$, for the Seasat and SIR-B R/V ratios. The dashed lines, asymptotically independent of significant wave height, represent the predicted

λ_o^4 assuming only velocities on spatial scales less than 50 m (twice the SAR spatial resolution for Seasat and SIR-B).

Note that, in general, the observed azimuth falloffs are significantly below values predicted in either (19) or (20). Assuming that velocities on spatial scales above 50 m do not contribute to azimuth smearing suggests a maximum λ_o, asymptotically approached at high sea states. The λ_o at high sea states, particularly for SIR-B spectra, appear to approach a constant at high sea states, but the data are not conclusive.

These numerical and analytic model estimates assume a broad-band fully developed sea. In SAR image spectra, we rarely observed fully developed seas. Much of the velocity variance is thus highly correlated to the swell wave slope and therefore does not contribute to azimuth smearing. Thus, the extent of azimuth smearing is somewhat less than expected purely on the basis of significant wave height and (19) and (20), and the simulations. The general leveling off of λ_o at high sea states in the data may simply indicate that the ocean is rarely fully developed at these high sea states.

Equations (19) and (20), and the simulation results when using broad-band input spectra therefore can be interpreted as upper bounds to λ_o. In all cases observed, λ_o has been found to be significantly lower although the dependence on R/V is corrected. For the case of SIR-B, even in the immediate region of Hurricane Josephine whose significant wave height was estimated at 8 m, λ_o was on the order of 100 m. For Seasat SAR image spectra from Hurricane Iva, having an estimated significant wave height of 6.5 m, the λ_o estimated from the SAR image spectrum was much larger, about 300 m.

VI. Conclusions

A procedure has been proposed to estimate ocean slope- and height-variance spectra from SAR imagery. Results, based on numerical simulation of SAR image spectra and comparisons between SAR image spectra from SIR-B and spectra measured by independent means, suggest that SAR image spectra, when multiplied by the appropriate linear transfer functions, produces accurate estimates of both the slope- and height-variance spectra. The resulting SAR spectra closely agree with independent measures of either the ocean wave slope and height-variance spectra.

The limitations of SAR image spectra at high azimuth wavenumbers in high sea-state conditions is directly proportional to the R/V ratio of the SAR platform. For R/V ratios of 35 s, typical of shuttle altitudes, significant azimuth spectral response extends to ocean wavelengths of at least 100 m in the highest expected sea states.

References

[1] R. C. Beal, D. G. Tilley, and F. M. Monaldo, "Large- and small-scale spatial evolution of digitally processed ocean wave spectra from the Seasat synthetic aperture radar," *J. Geophys. Res.*, vol. 88, pp. 1761-1778, 1983.

[2] R. C. Beal, T. W. Gerling, D. E. Irvine, F. M. Monaldo, and D. G. Tilley, "Spatial variations of ocean wave directional spectra from the Seasat synthetic aperture radar," *J. Geophys. Res.*, 1985.

[3] R. A. Shuchman and O. H. Shemdin, "Synthetic aperture radar imaging of ocean waves during the Marineland experiment," *IEEE J. Oceanic Eng.*, vol. OE-8, pp. 83-90, 1983.

[4] R. A. Shuchman, J. D. Lyden, and D. R. Lyzenga, "Estimates of ocean wavelength and direction from X- and L-band synthetic aperture radar during the Marineland experiment," *IEEE J. Oceanic Eng.*, vol. OE-8, pp. 90-96, 1983.

[5] W. Alpers and C. Bruening, "On the nonlinearity of the synthetic aperture radar response to moving ocean surface waves," *IEEE Trans. Geosci. Remote Sensing*, submitted for publication.

[6] F. M. Monaldo, "Improvement in the estimate of dominant wavenumber and direction from spaceborne SAR image spectra when corrected for ocean surface movement," *IEEE Trans. Geosci. Remote Sensing*, vol. GE-22, pp. 603-608, 1984.

[7] W. Alpers, D. B. Ross, and C. L. Rufenach, "On the detectability of ocean surface waves by real and synthetic aperture radar," *J. Geophys. Res.*, vol. 86, pp. 6481-6498, 1981.

[8] W. Alpers, "Monte Carlo simulation for studying the relationship between ocean wave and synthetic aperture radar image spectra," *J. Geophys. Res.*, vol. 88, pp. 1745-1759, 1983.

[9] D. R. Lyzenga, "Numerical simulations of synthetic aperture radar image spectra for ocean waves," *IEEE Trans. Geosci. Remote Sensing*, submitted for publication.

[10] E. J. Walsh, D. W. Hines, III, R. N. Swift, and J. F. Scott, "Directional wave spectra measured with the surface contour radar," *J. Phys. Oceanogr.*, vol. 15, p. 566, 1985.

[11] J. C. Jackson and W. T. Walton, "Aircraft and satellite measurement of ocean wave directional spectra using scanning-beam microwave radars," *J. Geophys. Res.*, vol. 90, pp. 987-1004, 1985.

[12] R. C. Beal, F. M. Monaldo, D. G. Tilley, D. E. Irvine, E. J. Walsh, F. C. Jackson, D. W. Hancock, III, D. E. Hines, R. N. Swift, F. I. Gonzalez, D. R. Lyzenga, and L. F. Zambresky, "A comparison of SIR-B directional wave spectra with aircraft scanning radar spectra and spectral ocean wave model predictions," *Science*, 1985.

[13] J. W. Wright, "Backscattering from capillary waves with application to sea clutter," *IEEE Trans. Antennas Propagat.*, vol. AP-14, pp. 749-754, 1966.

[14] O. M. Phillips, "The structure of short gravity waves on the ocean surface," in *Spaceborne Synthetic Aperture Radar for Oceanography*, R. C. Beal, P. S. DeLeonibus, and I. Katz, Eds. Baltimore, MD: The Johns Hopkins University Press, 1981.

[15] D. E. Irvine, "The interaction of long waves and short waves in the presence of wind," Ph.D. dissertation, The Johns Hopkins University, 1983.

[16] W. J. Plant, W. C. Keller, and A. Cross, "Parametric dependence of ocean wave-radar modulation transfer functions," *J. Geophys. Res.*, vol. 88, pp. 8747-9756, 1983.

[17] D. G. Tilley, "The use of speckle for determining the response characteristics of Doppler imaging radars," presented at the 29th Ann. Symp. Opt. Eng. Soc., San Diego, CA, Aug. 1985.

[18] A. D. Goldfinger, "Estimation of spectra from speckled images," *IEEE Trans. Aerosp. Electron. Syst.*, vol. AES-18, pp. 675-681, 1982.

[19] F. M. Monaldo and R. C. Beal, "Limitations of Seasat SAR in high sea states," in *Wave Dynamics and Radio Probing of the Sea Surface*, O. M. Phillips and K. Hasselmann, Eds. New York: Plenum, 1986, in press.

[20] M. J. Tucker, "The imaging of waves by satellite synthetic aperture radar: The effects of surface motion," *Int. J. Remote Sensing*, vol. 6, pp. 1059-1074, 1985.

[21] M. J. Tucker, "The decorrelation time of microwave radar echoes from the sea surface," *Int. J. Remote Sensing*, vol. 6, pp. 1075-1089, 1985.

[22] J. W. Wright, "Detection of ocean waves by microwave radar: The modulation of short gravity-capillary waves," *Bound.-Layer Meteorol.*, vol. 13, pp. 87-105, 1978.

[23] W. J. Pierson and L. Moskowitz, "A proposed spectral form for fully developed wind seas based in the similarity theory of S. A. Kitaigoroskii," *J. Geophys. Res.*, vol. 69, pp. 5181-5190, 1964.

Frank M. Monaldo was born in Washington, DC, in 1956. He received the B.A. and M.S. degrees, both in physics, from the Catholic University of America in 1977 and 1978, respectively.

In 1980, he was a visiting scientist at the Max Planck Institute for Meteorology in Hamburg, West Germany. Employed by the Johns Hopkins University Applied Physics Laboratory since 1977, he has concentrated on various aspects of remote sensing. The projects he has worked on include optical imaging of ocean waves from near surface platforms as well as synthetic aperture radar (SAR) imagery waves from spaceborne platforms. Besides work in interpretation of SAR data collected during the SIR-B shuttle mission in 1984, he is currently involved in evaluating potential errors arising from spaceborne radar altimetry and the development of advanced altimeter design concepts.

David R. Lyzenga received the B.S.E. degree in physics from the University of Michigan in 1967, the M.S. degree in physics from Yale University in 1968, and the Ph.D. degree in electrical engineering from the University of Michigan in 1973.

He taught mathematics and physics at Calvin College in 1968–1969, and worked at the Space Physics Research Laboratory of the University of Michigan from 1970 to 1972. Since 1973, he has been employed by the Environmental Research Institute of Michigan (ERIM), where he has engaged in a variety of remote-sensing projects involving both visible and microwave sensors. Since 1981, his primary research interest has been in the extraction of oceanographic information from synthetic aperture radar data. He is presently a Research Engineer in the Radar Science Laboratory at ERIM.

Dr. Lyzenga is a member of the American Geophysical Union, the Optical Society of America, Sigma Xi, Tau Beta Phi, and Phi Kappa Phi.

END

8-87

DTIC